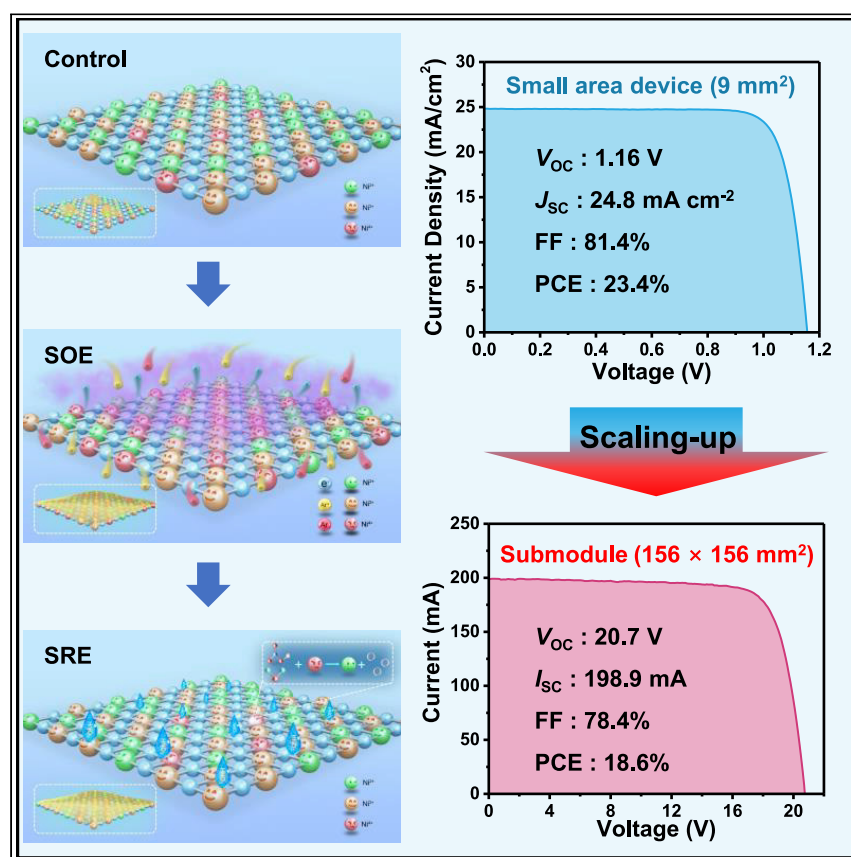


Article

Surface redox engineering of vacuum-deposited NiO_x for top-performance perovskite solar cells and modules



We propose a surface redox engineering (SRE) for NiO_x films, which is achieved by subjecting the films to an Ar-plasma-initiated oxidation process and a Brønsted-acid-mediated reduction process. The multifunctional SRE can foster the formation of a stabilized surface state and increase the surface energy. The assembled rigid (flexible) PSCs delivered high PCEs of up to 23.4% (21.3%) with excellent stability. Furthermore, large-area (156 × 156 mm²) submodules are designed and integrated to yield PCE as high as 18.6%.

Minyong Du, Shuai Zhao, Lianjie Duan, ..., Yantao Shi, Kai Wang, Shengzhong (Frank) Liu

wangkai@dicp.ac.cn (K.W.)
szliu@dicp.ac.cn (S.L.)

Highlights

High-performance NiO_x by large-area e-beam evaporation at room temperature

Facile SRE for NiO_x films to make the large-area slot-die-coated PSCs

SRE mechanism is revealed by experiments and theoretical simulations

SRE strategy improves the efficiency and stability of the solar cells

Du et al., Joule 6, 1931–1943

August 17, 2022 © 2022 Elsevier Inc.

<https://doi.org/10.1016/j.joule.2022.06.026>



Article

Surface redox engineering of vacuum-deposited NiO_x for top-performance perovskite solar cells and modules

Minyong Du,^{1,3,6} Shuai Zhao,^{2,6} Lianjie Duan,¹ Yuexian Cao,¹ Hui Wang,¹ Youming Sun,¹ Likun Wang,¹ Xuejie Zhu,⁴ Jiangshan Feng,⁴ Lu Liu,^{1,3} Xiao Jiang,¹ Qingshun Dong,⁵ Yantao Shi,⁵ Kai Wang,^{1,*} and Shengzhong (Frank) Liu^{1,3,4,7,*}

SUMMARY

It is arduous to prepare thin charge transport layers (CTLs) of only a few nanometers in thickness for meter-sized products, particularly for commonly used solution processes. Thus, it is desirable to take advantages of both solution-processed perovskites and vacuum-deposited CTLs. Herein, a surface redox engineering (SRE) is proposed for vacuum-deposited NiO_x to make it match with the slot-die-coated perovskite films. Not only does it eliminate the de-wetting problem of perovskite ink, but it also imparts enhanced electronic properties at buried interfaces. Consequently, high-performance PSCs are achieved with amazing stability and outstanding power conversion efficiencies of 23.4% and 21.3% for rigid and flexible devices, respectively. Furthermore, perovskite submodules of area $156 \times 156 \text{ mm}^2$ are successfully assembled with a remarkable PCE of 18.6% along with excellent stability. The SRE provides a strategy to use the advantages of both vacuum-fabricated CTLs with wet-processed perovskites for the development of large-area perovskite modules.

INTRODUCTION

State-of-the-art perovskite solar cells (PSCs) have glaringly entered the huge photovoltaic arena representing the most promising solar technology. The rapidly increasing power conversion efficiency (PCE) has exceeded 25% in a decade,¹ enabling PSCs to rival silicon solar cells and accelerating the wave of commercialization. Unequivocally, inverted PSCs are potentially more valuable than their normal counterparts because the former, with easily mitigated hysteresis behavior and long-term durability, are more compatible with commercial development.^{2–5} Recently, the certificated PCE of inverted PSCs has risen to 23.91% as reported by Sargent's group,⁶ which marginally lags those of normal devices.^{1,7} It is notable that wet-processed nickel oxide (NiO_x) nanoparticles were employed to extract holes in this record rather than the costly and labile organic semiconductors,^{3,8–11} substantiating the paramount value of NiO_x hole transport layers.

Although it has enabled the maximum PCE, wet-processed NiO_x generally requires an energy-intensive annealing process, and its quality tends to be sensitive to the synthesis conditions (e.g., ambient temp, solution pH, and stirring time), and thus, it suffers from poor reproducibility.^{12–17} More importantly, it is extraordinarily challenging to extend the fabrication of millimeter-size thin films as thin as $\sim 10 \text{ nm}$

Context & scale

Nickel oxide (NiO_x) is one of the most commonly used inorganic hole transport materials in inverted perovskite solar cells (PSCs) because of its outstanding stability and optical transmittance in entire visible spectrum. Unfortunately, its hydrophobicity and oxidizability badly affect uniform preparation of large-area stable devices. Here, we report a facile surface redox engineering (SRE) for electron-beam evaporated NiO_x to perfectly match the slot-die-coated large-area PSCs. This SRE strategy eliminates the local de-wetting problem of the perovskite ink and also imparts enhanced performance in electronic properties at the buried interface via modulating the NiO_x surface features. Consequently, high-performance PSCs are attained with power conversion efficiencies (PCEs) of 23.4% and 21.3% for rigid and flexible devices. Furthermore, the large-area ($156 \times 156 \text{ mm}^2$) perovskite submodules are successfully assembled with a remarkable PCE as high as 18.6%.



to the decimeter or meter size via current scalable technologies (e.g., slot-die coating, spray coating, and inkjet printing) while assuring uniformity.¹⁸ By contrast, dry vacuum processes with superior control over the film uniformity allow the effortless deposition of large-scale and pinhole-free films.¹⁹ In addition, vacuum-processed metal oxides are generally sub-stoichiometric with oxygen/metal deficiency since they will undergo redox reactions readily in the deposition chamber.²⁰ This feature is beneficial for NiO_x as the resulting point defects, along with its self-doping mechanism, and will lead to strong p-type character and high hole density. Compared with other vacuum processes, such as sputtering method,^{21–24} electron-beam evaporation (EBE) stands out as a mature and dominant method owing to its lower-cost equipment, low complexity, and damageless operation at room temperature.^{25–28} Recently, Abzieher et al. systematically controlled the EBE-NiO_x film composition through altering the deposition parameters, and yet the PSCs achieved only a mediocre PCE of 21.6% accompanied by stabilized power output of 18.5%, which is the maximum value for devices incorporating EBE-NiO_x.^{29,30} Therefore, this promising technology for NiO_x deposition still suffers from inferior performance in devices.

In addition to film composition, the interface state is also crucial to device performance and stability. For most vacuum-processed NiO_x films, the relatively hydrophobic surface attenuates the adhesion of perovskite ink,³¹ which marginally impacts the dynamic spin-coating process,³² but the evident de-wetting behavior that induces ink shrink and pin-hole issues in printing make it challenging to deposit large-area perovskite films. Even worse, the common hydrophilization methods (e.g., UV-ozone and O₂ plasma treatment) will decrease film transmittance and increase the density of sub-gap states.³³ Moreover, the surface chemistry of NiO_x is rather complex as a large number of high-oxidative-state Ni species (Ni³⁺ and Ni²⁺), and chemically reactive hydroxyls (NiOOH and –Ni(OH)₂) can decompose perovskites,^{34,35} leading to an interface energy barrier and non-capacitive hysteresis.^{36,37} To date, the developed surface engineering for NiO_x, mainly for wet-processed NiO_x, mostly adopts small molecules or costly p-type organic semiconductors to reduce interface defects and promote energy-level alignment.^{38–41} In turn, these strategies frequently decrease the interface tension, rendering the deployment for large areas more challenging, and meanwhile ignore the performance/stability degradation caused by interfacial reaction issues. Thus, it is highly desirable to develop a scalable surface strategy for EBE-NiO_x that can enable the surface to support optimal wettability for perovskite layer stacking and ensure a stable surface composition to achieve rapid hole dynamics, aimed at producing highly efficient NiO_x-PSCs.

Herein, we propose a method for surface redox engineering (SRE) of EBE-NiO_x films, which is achieved by subjecting the films to an Ar-plasma-initiated oxidation process and a Brønsted acid-mediated reduction process. We attempt to reveal the mechanism of this SRE by combining *in situ* characterizations with theoretical simulation and illuminate the chemical reactions comprising evident screening behavior. The multifunctional SRE can not only foster the formation of a stabilized surface state accompanied by increased conductivity and improved energy-band alignment but also increase the surface energy to improve the stacking of perovskite film on NiO_x. In this scenario, we successfully deposited large-area, full-coverage, high-quality perovskites on NiO_x via slot-die coating, and the assembled rigid (flexible) PSCs delivered high PCEs up to 23.4% (21.3%) with excellent stability. Furthermore, thanks to the scalability of this technology, large-area (156 × 156 mm²) perovskite solar submodules were configured and yielded a PCE as high as 18.6%. The current

¹Dalian National Laboratory for Clean Energy, iChEM, Dalian Institute of Chemical Physics, Chinese Academy of Sciences, Dalian 116023, Liaoning, China

²School of Science, Chongqing University of Technology, Chongqing 400054, China

³University of the Chinese Academy of Sciences, Beijing 100039, China

⁴Key Laboratory of Applied Surface and Colloid Chemistry, Ministry of Education, Shaanxi Key Laboratory for Advanced Energy Devices, Shaanxi Engineering Lab for Advanced Energy Technology, Institute for Advanced Energy Materials, School of Materials Science and Engineering, Shaanxi Normal University, Xi'an 710119, China

⁵State Key Laboratory of Fine Chemicals, Department of Chemistry, School of Chemical Engineering, Dalian University of Technology, Dalian 116024, China

⁶These authors contributed equally

⁷Lead contact

*Correspondence: wangkai@dicp.ac.cn (K.W.), szliu@dicp.ac.cn (S.L.)

<https://doi.org/10.1016/j.joule.2022.06.026>

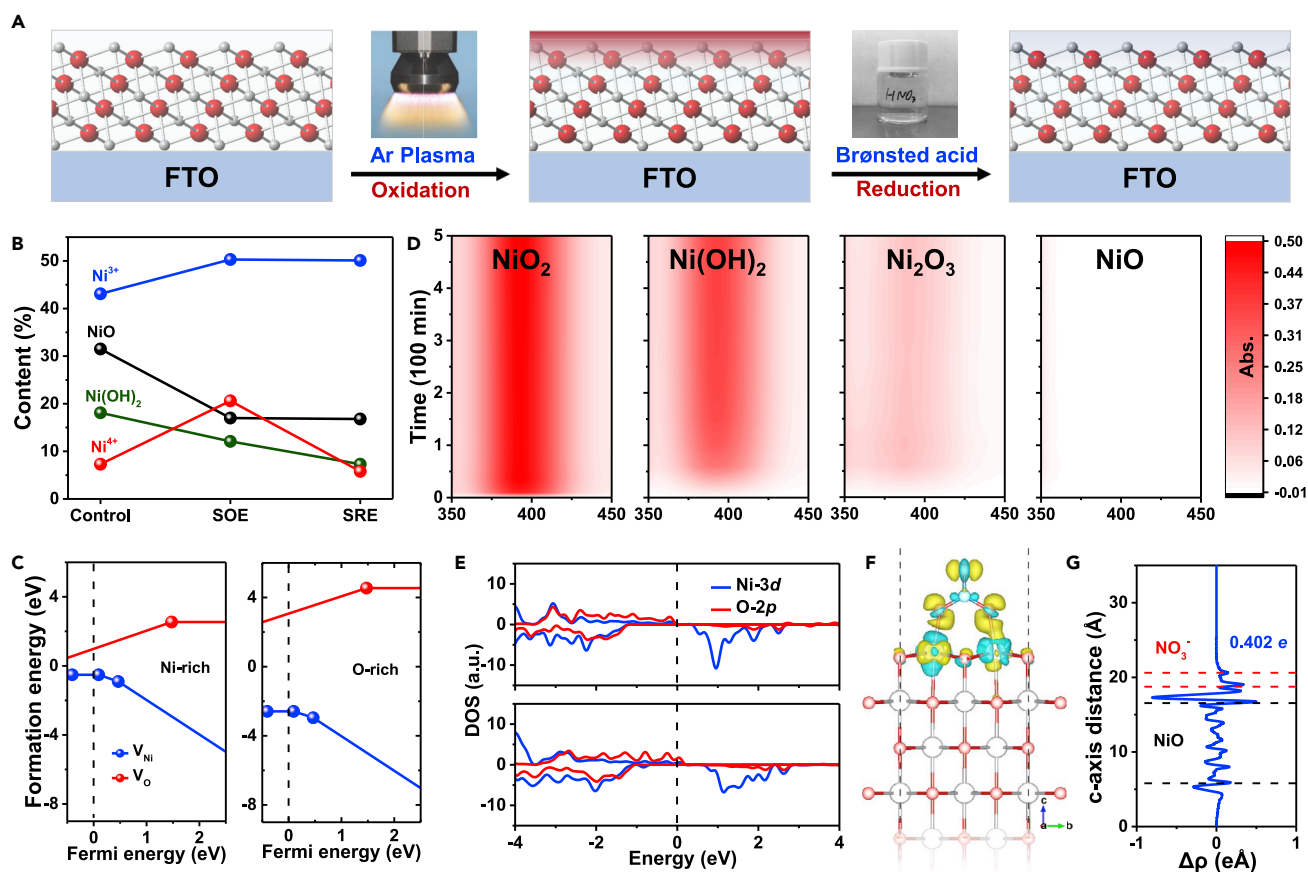


Figure 1. The influence and mechanism of SRE

(A) Schematic illustration showing the process of SRE.

(B) The variation of Ni species caused by SRE.

(C) Calculated formation energies of Ni and O vacancies as a function of the Fermi energy under Ni-rich and O-rich conditions.

(D) UV-vis absorption spectra of solutions of NiO₂/Ni(OH)₂/Ni₂O₃/NiO powder dissolved in 3 M HNO₃ (x axis is wavelength).

(E–G) (E) Density of states, (F) optimized NiO surface structure, and (G) planar-averaged charge density difference of NiO surface with NO₃[−] adsorption.

SRE provides a way for the surface regulation of vacuum-processed NiO_x films, and the proof of concept combining vacuum-processed NiO_x with wet-processed perovskites will promote the industrialization of perovskite solar modules.

RESULTS AND DISCUSSION

The influence and mechanism of SRE

Figure 1A depicts the SRE process for NiO_x films that first undergo a nonthermal Ar plasma environment to enhance the surface wettability. This process is named surface oxidation engineering (SOE) for NiO_x, which will be rationalized in the following. Note that we have compared Ar plasma with UV ozone and O₂ plasma as shown in Figure S1. They all can darken the films in a few minutes, except Ar plasma, which takes a prolonged time. Second, the films were exposed in facile Brønsted acid (where nitric acid is employed herein), which can bleach the films through a mechanism to be revealed. Notably, both the EBE and SRE are executed at room temperature.

Figures S2A and S2B illustrate the X-ray photoemission spectroscopy (XPS) spectra to elucidate the SRE-dependent variation of surface moieties on NiO_x

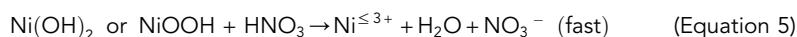
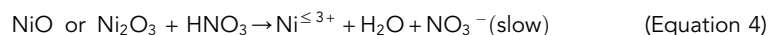
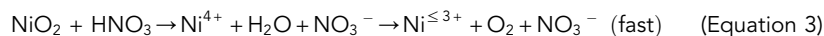
films. The Ni2p_{3/2} and O1s core-level envelopes were separated according to the literature as summarized in [Tables S2](#) and [S3](#). According to the literature, for the control and SOE-NiO_x, the peaks located at 853.60, 854.45, 855.60, and 856.85 eV pertain to Ni²⁺ in the integral NiO lattice, Ni(OH)₂, Ni³⁺ (including Ni₂O₃ and NiOOH), and Ni⁴⁺, respectively.^{22,36} An additional peak positioned at 854.10 eV belongs to Ni(NO₃)₂ for the SRE-NiO_x. Note that, in addition to the NiO backbone, Ni³⁺ benefits the semiconductor properties, while the susceptible Ni⁴⁺ is detrimental to the perovskite layer due to its strong oxidizing property, and –OH specie may trigger the deprotonation of perovskites.⁴² [Figure 1B](#) shows the variation in the content of different Ni species. Upon SOE, both the concentrations of Ni³⁺ and Ni⁴⁺ increase, whereas there is a drop off in the percentage of NiO and Ni(OH)₂ species. Videlicet, the energetic Ar plasma initiates an oxidizing process from the low-valent state of NiO and Ni(OH)₂ to the high-valent state Ni^{≥3+}. We inferred that the high-energy bombardment would dissociate the chemical bonds between the lattice O^{2–} and Ni²⁺ and cause atomic displacement, thus easily generating Ni²⁺ vacancy defects in the Ar plasma conditions. One Ni²⁺ vacancy results in the formation of two Ni³⁺ ions or one Ni⁴⁺ to maintain charge neutrality, dramatically triggering the films to be largely composed of increased oxidation states. To support this inference, we predict the formation energy of Ni²⁺ vacancy and O^{2–} vacancy through density functional theory (DFT) calculation. Note that, dissimilar to other oxides (such as TiO₂, ZnO, MoO_x, WO_x, and SnO₂),^{43,44} Ni vacancies are frequent defects in NiO as evidenced by its inferior formation energy compared with O^{2–} vacancies under either Ni or O-rich conditions ([Figure 1C](#)). Furthermore, the Ni²⁺ ions freed by the bombardment may escape into the vacuum or be chemisorbed near surface defects and then react with O₂ or H₂O in the air to form NiO or Ni(OH)₂ due to the low thermodynamic potential $E_{\text{Ni}^{2+}/\text{Ni}}^{\ominus} = -0.257$ V versus $E_{\text{O}_2/\text{H}_2\text{O}}^{\ominus} = 1.229$ V. The presumed chemical equations are as follows:



This assumption is also in excellent agreement with the increased O/Ni ratio upon SOE ([Figure S2C](#)). As for the reduced Ni(OH)₂ content, the energy of a dozen electron volts⁴⁵ in Ar plasma is sufficient to convert Ni(OH)₂ to NiOOH since they possess an identical rhombohedral structure.³⁴ Thus, Ar plasma treatment can not only increase surface wettability ([Figure S3](#)) but also initiate the surface oxidation process and induce the formation of detrimental Ni⁴⁺ species.

Upon further modifying the surface with Brønsted acid, the contents of Ni(OH)₂ and Ni⁴⁺ significantly decline, while those of NiO and Ni³⁺ remain constant. Thus, acid can selectively eliminate the detrimental Ni⁴⁺ and –OH but reserve the beneficial Ni³⁺ and NiO backbone. To explain the screening behavior of acid, the reaction dynamics were tracked via the UV-visible absorption spectra, whereby NiO₂, Ni₂O₃, NiO, and Ni(OH)₂ powder were used as model compounds in acid. As per [Figure 1D](#), the order of chemical reaction activity is Ni⁴⁺ > Ni(OH)₂ ≫ Ni³⁺ > NiO. We also observed that NiO₂ is inert in water, whereas it reacts violently with acids and generates numerous bubbles. Combining the high thermodynamic potential $E_{\text{NiO}_2/\text{Ni}^{2+}}^{\ominus}$ (1.68 V) versus $E_{\text{O}_2/\text{H}_2\text{O}}^{\ominus}$ (1.23 V), we rationally infer that Ni⁴⁺ in the lattice will first convert into free Ni⁴⁺ ions in the acid, which then oxidizes water into O₂ accompanied by the formation of Ni^{≤3+}. In addition, Ni(OH)₂ is converted into Ni(NO₃)₂ in

the Brønsted acid environment. All the reactions can be described by the following equations:



Therefore, Brønsted acid capably mediates a reduction reaction for NiO_x to selectively eliminate detrimental Ni^{4+} and neutralize the surface hydroxyl. In addition, Figure S2C presents the calculated $\text{Ni}^{3+}/\text{Ni}^{2+}$ ratios for the control, SOE, and SRE samples, which are 0.87, 1.73, and 2.08, respectively. The evidently rising $\text{Ni}^{3+}/\text{Ni}^{2+}$ ratio in NiO_x inevitably implies the reinforced p-type semiconductor property of SRE- NiO_x film.¹⁷ Furthermore, according to the DFT calculation, the adsorption energy of NO_3^- on the NiO surface was predicted to be -2.90 eV, indicating energetically favorable adsorption. As per the density of states in Figure 1E, the pristine NiO surface shows a semi-conductive electronic structure, similar to the bulk NiO. Upon adsorbing NO_3^- (Figure 1F), the d electrons of surface Ni^{2+} cations transfer to the NO_3^- group, leading to a decrease of the Fermi energy level. Moreover, the NO_3^- adsorption triggers charge reorganization, whereby ~ 0.402 electron transfers from the NiO to the NO_3^- group (Figure 1G), which may increase the conductivity of the top NiO layer and induce an interfacial dipole, thus facilitating the hole injection process. Collectively, SRE for NiO_x provides three functions: reducing surfacing tension, stabilizing the surface and enhancing the surface electrical properties.

The scanning electron microscopy (SEM) images, atomic force microscopy (AFM) images, UV-visible absorption, and transmittance spectra of various NiO_x films in Figures S4–S6 manifest the identical morphology of the films with ~ 11 -nm roughness and optical transmittances with a band gap of 3.68 eV regardless of SRE. Figure S7 shows the conducting-AFM (C-AFM) maps for various NiO_x films. The gradually increasing average current in the order of control-, SOE-, SRE- NiO_x implies enhanced conductivity, consistent with the $\text{Ni}^{3+}/\text{Ni}^{2+}$ ratio variation. In addition, the Hall effect measurement reveals that the hall mobility increases from 1.38 to 1.47 and to $1.65 \text{ cm}^2 \text{ V}^{-1} \text{ s}^{-1}$ for the control, SOE, and SRE samples. In the meantime, the carrier density also increases from 2.40×10^{15} to 2.42×10^{15} and to $2.84 \times 10^{15} \text{ cm}^{-3}$ for the control, SOE, and SRE samples, which are competitive with the previous results.²² These results also imply that SRE may also alter the compositions within a certain depth of the film, similar to the effect of UV-ozone treatment reported by Islam et al.³³ In parallel, the Kelvin probe force microscopy (KPFM) results in Figure S8 also demonstrate the rising work function from -0.34 to -0.71 and to -0.75 V for the control, SOE, and SRE samples. This cascade shift potentially leads to improved band alignment along with smaller voltage loss at the heterojunctions and enhanced charge extraction.⁴⁶ Note that both the increments in the conductivity and work function are contributed by the enhanced p-type semiconductor property, which are in line with the XPS analysis and DFT calculations.

Effect of SRE on perovskite films

Have revealed the SRE mechanism on NiO_x films, we deposited perovskite layers via slot-die coating; all the perovskite films hereafter were prepared with this method. As per Figures S3 and S9, the contact angle of a perovskite droplet on pristine

NiO_x films is $\sim 40.6^\circ$, which is sufficient for achieving uniform perovskite layers via spin-coating. However, the slot-die coated perovskite layers on pristine NiO_x films are full of clusters and large exposed regions, even on the small substrates, due to the local de-wetting issue and spontaneous shrink of perovskite wet films. Thus slot-die coating technology has higher requirements for wettability than spin-coating. Upon SOE or SRE, the surface-free energy increases, and the contact angle was mitigated to $\sim 7^\circ$; then, the adhesion between the perovskite ink and underlying NiO_x surface is improved, and thus the slot-die coated perovskite film is uniform in appearance with nearly 100% coverage. Moreover, the wettability will affect the crystallization of perovskite films according to the association between the free energy (G) for heterogeneous and homogeneous nucleation:

$$G_{\text{Heterogeneous}} = G_{\text{Homogeneous}} \times \frac{(2 + \cos \theta)(1 - \cos \theta)^2}{4} \quad (\text{Equation 6})$$

where θ is the contact angle on the solid/liquid interface. The smaller θ of perovskite ink on SRE-NiO_x results in a lower energy barrier for heterogeneous nucleation, which promotes the formation of uniform and high-quality perovskite films. XRD patterns in Figure S10 show that both the diffraction intensity of the perovskite films and the texture coefficient of the (101) plane increase gradually in the order of control, SOE and SRE, signifying the gradually increased crystallinity and higher degree of preferred orientation. Figure S11 shows top-view SEM images of perovskite films on various substrates. The perovskite films on pristine NiO_x films possess a large number of pinholes at grain boundaries, which will serve as pathways for charge recombination and initiating sites for degrading device performance. On the contrary, both SOE and SRE enable compact perovskite films with significantly diminished pinholes and enlarged grain sizes together with reduced defect density, thus achieving the prerequisite for high-efficiency devices.

Photovoltaic performance and stability of perovskite solar cells

Given these significant improvements to the surface and perovskite crystals, small-area PSCs were initially assembled with the structure FTO/NiO_x/perovskite/[6,6]-Phenyl-C₆₁-butyric acid methyl ester/bathocuproine/Ag. Figure 2A is a cross-sectional SEM image of an integral device with labeled layers. The photovoltaic parameters are summarized in Table S4, and the statistical histogram of PCE is depicted in Figure S12. The average PCEs for the control, SOE and SRE PSCs are $18.0\% \pm 0.9\%$, $20.3\% \pm 0.4\%$ and $22.7\% \pm 0.4\%$ (Table S5), respectively. The step-wise rising PCE along with decreased scattering is contributed by the synchronously increased open-circuit voltage (V_{OC}) and fill factor (FF) rather than the similar short-circuit current density (J_{SC}), signifying the powerful effect of SRE for facilitating interface hole dynamics. The significantly improved parameters are attributed to the stabilized surface with better electrical properties and improved band alignment as well as the optimized perovskite polycrystalline films. Strikingly, Figure 2B shows the current density-voltage (J-V) curves (forward and reverse scans) for the champion SRE PSCs, which delivered a reverse-scan PCE as high as 23.4%, entailing a V_{OC} of 1.16 V, J_{SC} of 24.8 mA cm^{-2} and FF of 81.4% along with negligible hysteresis and a steady-state maximum power point (MPP) efficiency of 22.7% under the bias of 0.96 V (Figure 2C). Since all the functional layers were prepared at low temperature $< 110^\circ\text{C}$, the entire recipe was effortlessly transferred for assembling flexible PSCs on polyethylene terephthalate coated by ITO with MgF₂ antireflection, which yielded a high V_{OC} of 1.09 V, J_{SC} of 24.5 mA cm^{-2} , and FF of 79.7%, thus leading to a maximum PCE of 21.3% with minimal hysteresis. (The average parameters are summarized in Table S6.) Note that both PCEs are among the highest for NiO_x-based rigid and flexible PSCs via scalable technologies (Figure 2D; Table S7). In addition,

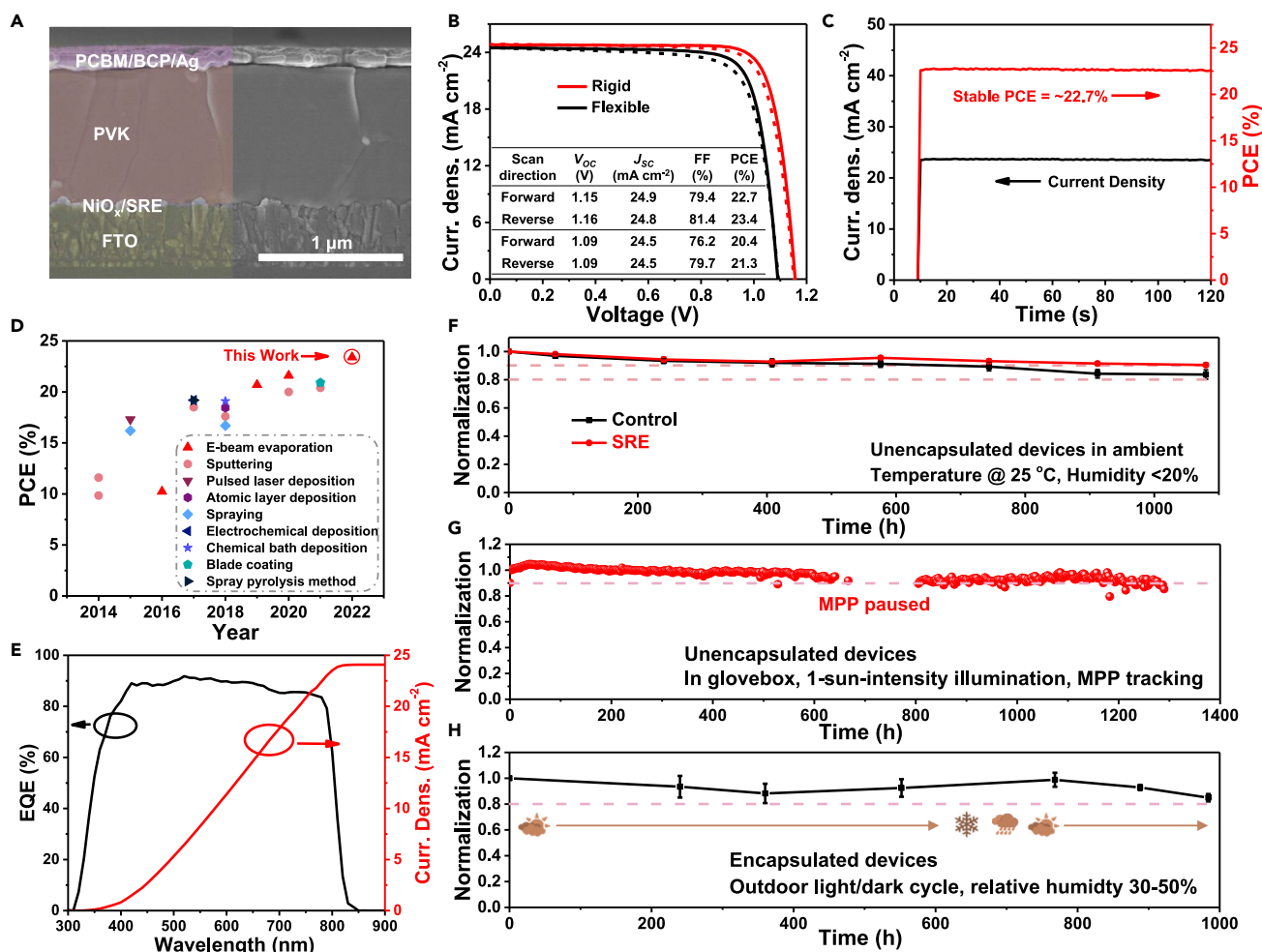


Figure 2. Performance of perovskite solar cells with SRE

(A) Cross-sectional SEM image of a PSC.
 (B) J-V curves of champion rigid/flexible devices.
 (C) Steady-state power and current output of a rigid PSC.
 (D) PCEs of NiO_x -PSCs prepared using scalable technologies.
 (E) EQE curve.
 (F–H) Long-term stability of devices measured under various conditions.

as per Figure 2E, the integrated J_{SC} extracted from the external quantum efficiency (EQE) of the device is 24.1 mA cm^{-2} , which is consistent with the values obtained from J-V curves.

Organic lead-halide perovskites with ionic nature and low formation energy are prone to degrade and are especially susceptible to light, thermal, moisture, or electric-field stress, which deteriorates the PCE and restricts the leveled cost of energy of PSCs. The interface plays a crucial role in stabilizing PSCs.^{47–53} We first examined the stability of unsealed devices in the laboratory environment (25 °C, relative humidity < 20%). As per Figure 2F, after ~1,100 h of aging, an SRE-PSC showed an obvious advancement in shelf-life stability and retained 90% of the initial PCE, whereas the conservation rate decreased to 83% for the control device. The operational stability of PSCs is measured under MPP tracking under continuous one-sun illumination. It was found that the SRE-PSC shows a T_{90} lifetime exceeding 1,300 h, demonstrating

outstanding long-term operational stability (Figure 2G). Besides aging in the laboratory, it is imperative to understand the degradation behavior under real outdoor conditions with extreme weather and climatic changes. As shown in Figure 2H, encapsulated SRE devices were aged in outdoor conditions (Dalian, winter, January to February), undergoing various weather conditions including light/dark, low temperature, rain, and snow. The PSCs degraded by 20% after $\sim 1,000$ h, equal to more than 41 natural diurnal cycles. The robust ambient and operational stability of these SRE devices can be attributed to the following reasons: (1) the hydroxyl groups of the pristine NiO_x surface decompose the perovskite into PbI_2 , FA, I^- , and H_2O via the degradation reactions $\text{FAPbI}_3 + \text{OH}^- \rightarrow \text{PbI}_2 + \text{FA} + \text{H}_2\text{O} + \text{I}^-$. The generated water would further accelerate the decomposition process. The acidified surface formed by replacing OH^- with NO_3^- will impair the deprotonating capability toward organic cations. (2) Another stability risk of the pristine NiO_x /perovskite interface is the oxidation of perovskites via the reaction $\text{Ni}^{>3+} + \text{I}^- \rightarrow \text{Ni}^{2+} + \text{I}_2$. Such issue is tackled by the acid-mediated reduction reaction. Additionally, the enhanced crystallinity and enlarged grain size of the perovskite layers also render the devices more stable.

Improved carrier dynamics on the surface of SRE- NiO_x film

The improved photovoltaic parameters and stability are related to the SRE-enhanced NiO_x surface and the advanced perovskite films grown on it. Numerous measurements were carried out to gain insight into the influence of SRE on the interface carrier dynamics. Figure S13 shows the UV-vis absorption and photoluminescence (PL) spectra of perovskite films deposited on NiO_x . In addition to the analogical absorption, SRE- NiO_x confers greater PL quenching on the perovskites in comparison with the control sample. Meanwhile, the time-resolved PL spectra of perovskite films on SRE- NiO_x also show a shorter decay time than the control (135 versus 360 ns), as shown in Figure 3A and Table S8. These results indicate that the interfacial hole transfer dynamics are effectively enhanced upon SRE. Given the close relation between charge dynamics and trap states, the space charge-limited current model was utilized for hole-only devices to quantitatively evaluate the density of trap states at the NiO_x /perovskite interface. From the dark J - V curves in Figure 3B, the trap-filled limit voltages (V_{TFL}) were measured to be 0.37 and 0.20 V for the control and SRE devices, respectively. Then the calculated trap density for the SRE device is $\sim 1.70 \times 10^{15} \text{ cm}^{-3}$ according to previous report,⁵⁴ which is relatively lower than that of the pristine one ($\sim 3.14 \times 10^{15} \text{ cm}^{-3}$). Figure 3C shows the capacitance-potential curves of control and SRE PSCs. The built-in potential (V_{bi}) evaluated through Mott-Schottky analysis increases from 1.11 V for the control to 1.21 V for the SRE PSCs. The enlarged V_{bi} will not only accelerate the dissociation of photogenerated carriers but also promote the construction of an extended depletion region to powerfully suppress nonradiative recombination. The Nyquist plots in Figure S14A were generated from measurements over a sequence of positive potentials in the dark.^{55,56} The equivalent-circuit model in the inset was used to fit the plots, where the sum of R_1 and R_2 refers to the recombination resistance R_{rec} ,⁵⁶ and C_s represents the surface charge accumulation capacitance at the contact/perovskite interface.⁵⁷ As depicted in Figures 3D and S14B, the higher R_{rec} and lower C_s in SRE PSCs manifest the suppressed charge recombination process and inhibited interface charge accumulation. Thermal admittance spectroscopy was performed to examine the trap density of states (tDOS) in PSCs. As per Figure 3E, the pristine device shows a relatively large tDOS on the order of 10^{16} – $10^{20} \text{ cm}^{-3} \text{ eV}^{-1}$. Upon SRE, the tDOS beyond 0.5 eV is lower by more than an order of magnitude, indicating that SRE could efficiently reduce the density of deep-level trap states both at the grain boundaries and interfaces. The light-intensity (I) dependence of J_{SC} and V_{OC} was measured to estimate recombination behaviors. Figure S15 displays the power law dependence of J_{SC} on I ($J_{\text{SC}} \propto I^n$) for both samples,

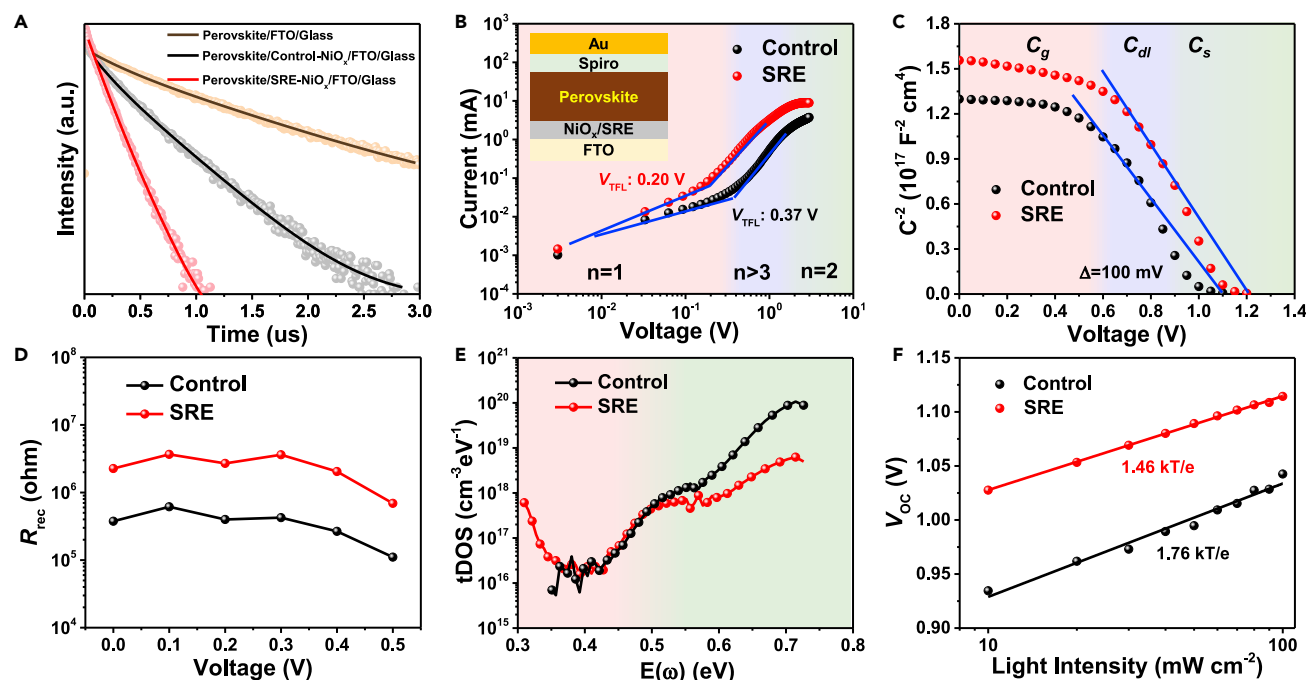


Figure 3. Interaction effect of SRE on the perovskite film and devices

(A) Time-resolved PL decay curves of perovskite films on FTO glass and control- and SRE-NiO_x films.
(B) Dark current-voltage curves of hole-only devices based on control- and SRE-NiO_x films.
(C) Mott-Schottky plots.
(D) R_{rec} as a function of the bias.
(E) Trap density of states and (F) V_{OC} versus light-intensity curves for PSCs with and without SRE.

where the factor α approaching 1 signifies a negligible space charge effect in both devices.⁵⁸ Figure 3F shows that the V_{OC} varies linearly with the logarithm of I . The deviation between the slope and kT/q (where k , T , and q are the Boltzmann constant, temperature, and elemental charge, respectively) positively correlates with Shockley-Read-Hall recombination.⁵⁹ It appears that the SRE devices possess evidently suppressed trap-assisted recombination, as reflected by the smaller slope, which is consistent with the increased V_{OC} and FF.

Efficient and stable perovskite submodules with SRE

We further evaluated the compatibility of SRE-NiO_x with the scaling up of the processes by fabricating perovskite submodules on substrates with area of $156 \times 156 \text{ mm}^2$. The details of the process for the perovskite submodules were described in the supplemental information and Video S1. It is worth noting again that we could not obtain uniform large-area perovskite films without SRE as shown in Figure S16. The modules were composed of 20 subcells of 7 mm width in series, and the interconnection was accomplished with laser-patterned P1, P2, and P3 channels; the geometrical FF is $\geq 85.7\%$ (Figure S17). As per Figure 4A, the active-area (174 cm^2) PCE of the champion submodule is 18.6% ($V_{OC} = 20.74 \text{ V}$; $I_{SC} = 198.9 \text{ mA}$; and FF = 78.4%) along with negligible hysteresis, as evidenced by the overlapped I - V curves measured in the reverse/forward scan directions. For each subcell with an area of 8.7 cm^2 in the champion submodule, the V_{OC} and J_{SC} are 1.04 V and 22.9 mA cm^{-2} , respectively. In comparison with small-area devices, we attributed this V_{OC} loss to the deficient laser power that induced a discontinuous P3 line, and the J_{SC} loss is triggered by the slightly attenuated perovskite film

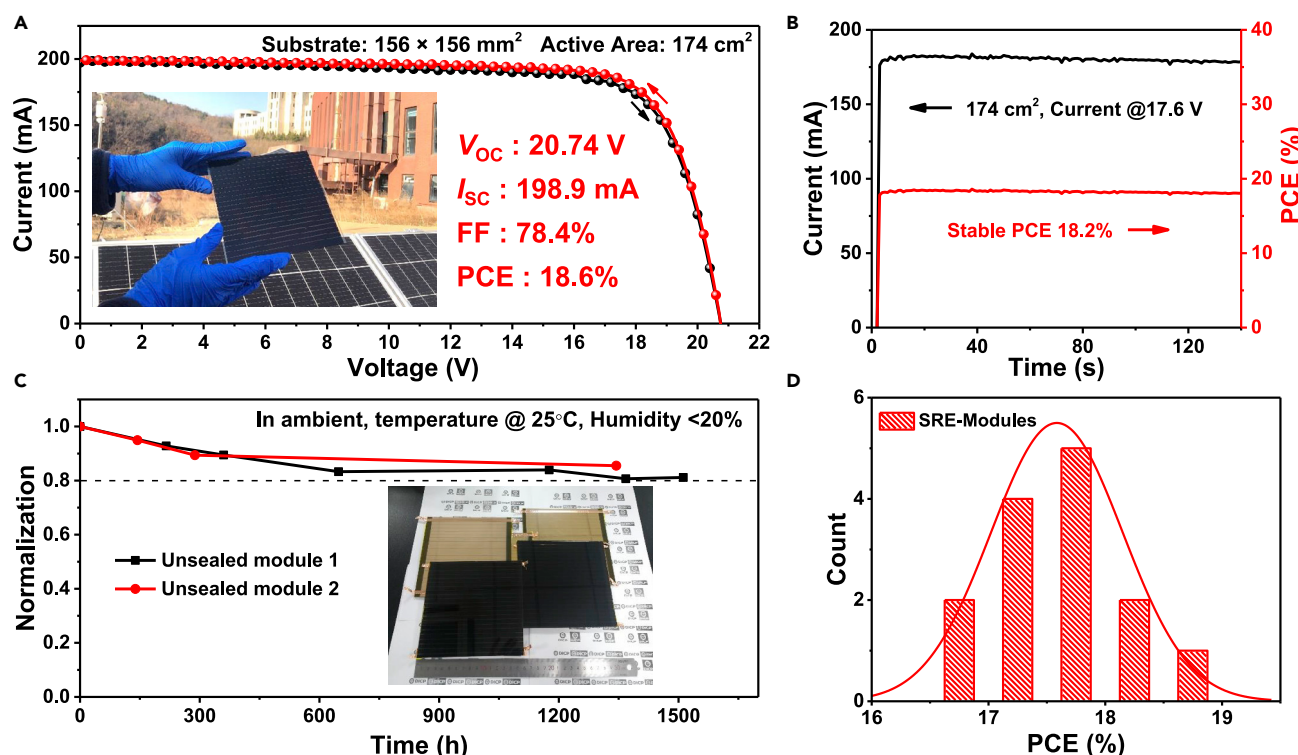


Figure 4. Performance of perovskite solar submodules

(A) *I*-*V* curves of the champion module measured in the reverse and forward scan directions.
 (B) Steady-state power output of the module at a fixed bias of 17.6 V for 140 s.
 (C) Long-term stability of two modules aged in the ambient environment.
 (D) PCE distribution of 14 modules.

thickness to lower the difficulty level of laser etching. We deduced this can be dramatically improved by optimizing the laser etching technique. Figure 4B shows the stabilized power output of the submodule, which delivers a stabilized PCE of 18.2% for 140 s. In addition, the submodules show excellent long-term shelf-life stability, retaining 80% of the initial performance upon aging in the dark for 1,500 h (Figure 4C). Additionally, the perovskite submodules showed excellent reproducibility (Figure 4D; Table S9), where ~21% and ~86% of modules realized PCEs of more than 18.0% and 17.0%, respectively. The outstanding module efficiency and stability originate from the good uniformity of the functional layers, the reduced interfacial trap density, and suppressed interfacial recombination.

Conclusions

In summary, a facile SRE process was proposed that not only enables slot-coating of perovskites on EBE-NiO_x film but also improves the properties and stability of the interface between the NiO_x and perovskite. Theoretical and experimental results reveal the redox reaction in the SRE induced variation of the surface moieties. Afterward, the SRE obviously improved the carrier transport and reduced the trap-assisted recombination in PSCs, boosting the device performance to 23.4% and 21.3% for rigid and flexible devices, respectively, while ensuring long-term stabilities over 1,000 h. Strikingly, the SRE was further extended to perovskite submodules, which demonstrate outstanding photovoltaic performance with PCE of 18.6% on 156 × 156 mm² substrates. Overall, the SRE connecting slot-die-coated perovskites to EBE-NiO_x will facilitate the commercialization of efficient and stable perovskite modules.

EXPERIMENTAL PROCEDURES

Resource availability

Lead contact

Further information and requests for resources should be directed to and will be fulfilled by the lead contact, Shengzhong (Frank) Liu (szliu@dicp.ac.cn).

Materials availability

This study did not generate new unique reagents.

Data and code availability

This study did not generate or analyze any datasets or codes. The data and results supporting the current study are available from the lead contact upon reasonable request.

SUPPLEMENTAL INFORMATION

Supplemental information can be found online at <https://doi.org/10.1016/j.joule.2022.06.026>.

ACKNOWLEDGMENTS

This work was supported by the Strategic Priority Research Program of the Chinese Academy of Sciences (grant no. XDA17040506), the National Nature Science Foundation of China (U20A20252, U21A20102, and 62174103), the Innovation Fund Project of Dalian Institute of Chemical Physics (DICP I202025, DICP I202032), the Cooperation Foundation of Dalian National Laboratory For Clean Energy of the Chinese Academy of Sciences (DNL202015), the Natural Science Foundation of Liaoning Province (2021-MS-016), the Youth Science and Technology Star Project of Dalian (2021RQ121), the 111 Project (B1404), the Project of Knowledge Innovation Engineering (Y261261606), the Transformational Technologies for Clean Energy and Demonstration, Strategic Priority Research Program of the Chinese Academy of Sciences (XDA21061001 and XDA21061002), the Fundamental Research Funds for the Central Universities (GK202103106), and the Shanxi Science and Technology Department (20201101012).

AUTHOR CONTRIBUTIONS

S.F.L., K.W., and M.D. proposed the project. M.D., L.D., and Y.C. fabricated the devices. M.D., L.D., Y.C., Y.S., J.F., Q.D., and Y.S. carried out the material and device characterizations. H.W., L.W., X.Z., L.L., and X.J. contributed useful comments for the paper. S.Z. performed the simulations. M.D. and K.W. analyzed all experimental data. M.D., K.W., and S.F.L. wrote the manuscript with discussion and input from all the authors. S.F.L. and K.W. supervised the overall project, discussed the results, and contributed to the final manuscript.

DECLARATION OF INTERESTS

The authors declare no competing interests.

Received: May 2, 2022

Revised: June 2, 2022

Accepted: June 22, 2022

Published: July 21, 2022

REFERENCES

1. NREL (2022). Best Research-Cell Efficiency Chart. <https://www.nrel.gov/pv/cell-efficiency.html>. (NREL)
2. Chen, S., Xiao, X., Gu, H., and Huang, J. (2021). Iodine reduction for reproducible and high-performance perovskite solar cells and modules. *Sci. Adv.* 7, eabe8130.
3. Wang, H., Huang, Z., Xiao, S., Meng, X., Xing, Z., Rao, L., Gong, C., Wu, R., Hu, T., Tan, L., et al. (2021). An *in situ* bifacial passivation strategy for flexible perovskite solar module with mechanical robustness by roll-to-roll fabrication. *J. Mater. Chem. A* 9, 5759–5768. <https://doi.org/10.1039/D0TA12067G>.
4. Bush, K.A., Palmstrom, A.F., Yu, Z.J., Boccard, M., Cheacharoen, R., Mailoa, J.P., McMeekin, D.P., Hoye, R.L.Z., Bailie, C.D., Leijtens, T., et al. (2017). 23.6%-efficient monolithic perovskite/silicon tandem solar cells with improved stability. *Nat. Energy* 2, 17009. <https://doi.org/10.1038/nenergy.2017.9>.
5. Xiao, K., Lin, R., Han, Q., Hou, Y., Qin, Z., Nguyen, H.T., Wen, J., Wei, M., Yeddu, V., Saidaminov, M.I., et al. (2020). All-perovskite tandem solar cells with 24.2% certified efficiency and area over 1 cm² using surface-anchoring zwitterionic antioxidant. *Nat. Energy* 5, 870–880. <https://doi.org/10.1038/s41560-020-00705-5>.
6. Chen, H., Teale, S., Chen, B., Hou, Y., Grater, L., Zhu, T., Bertens, K., Park, S.M., Atapattu, H.R., Gao, Y., et al. (2022). Quantum-size-tuned heterostructures enable efficient and stable inverted perovskite solar cells. *Nat. Photonics* 16, 352–358. <https://doi.org/10.1038/s41566-022-00985-1>.
7. Yoo, J.J., Seo, G., Chua, M.R., Park, T.G., Lu, Y., Rotermond, F., Kim, Y.K., Moon, C.S., Jeon, N.J., Correa-Baena, J.P., et al. (2021). Efficient perovskite solar cells via improved carrier management. *Nature* 590, 587–593. <https://doi.org/10.1038/s41586-021-03285-w>.
8. Li, F., Deng, X., Qi, F., Li, Z., Liu, D., Shen, D., Qin, M., Wu, S., Lin, F., Jang, S.H., et al. (2020). Regulating surface termination for efficient inverted perovskite solar cells with greater than 23% efficiency. *J. Am. Chem. Soc.* 142, 20134–20142. <https://doi.org/10.1021/jacs.0c09845>.
9. Zheng, X., Hou, Y., Bao, C., Yin, J., Yuan, F., Huang, Z., Song, K., Liu, J., Troughton, J., Gasparini, N., et al. (2020). Managing grains and interfaces via ligand anchoring enables 22.3%-efficiency inverted perovskite solar cells. *Nat. Energy* 5, 131–140.
10. Calió, L., Kazim, S., Grätzel, M., and Ahmad, S. (2016). Hole-transport materials for perovskite solar cells. *Angew. Chem. Int. Ed. Engl.* 55, 14522–14545. <https://doi.org/10.1002/anie.201601757>.
11. Li, X., Zhang, W., Guo, X., Lu, C., Wei, J., and Fang, J. (2022). Constructing heterojunctions by surface sulfidation for efficient inverted perovskite solar cells. *Science* 375, 434–437. <https://doi.org/10.1126/science.abc5676>.
12. Zhu, Z., Bai, Y., Liu, X., Chueh, C.C., Yang, S., and Jen, A.K. (2016). Enhanced efficiency and stability of inverted perovskite solar cells using highly crystalline SnO₂ nanocrystals as the robust electron-transporting layer. *Adv. Mater.* 28, 6478–6484. <https://doi.org/10.1002/adma.201600619>.
13. Wu, Y., Xie, F., Chen, H., Yang, X., Su, H., Cai, M., Zhou, Z., Noda, T., and Han, L. (2017). Thermally stable MAPbI₃ perovskite solar cells with efficiency of 19.19% and area over 1 cm² achieved by additive engineering. *Adv. Mater.* 29, 1701073. <https://doi.org/10.1002/adma.201701073>.
14. Yin, X., Chen, P., Que, M., Xing, Y., Que, W., Niu, C., and Shao, J. (2016). Highly efficient flexible perovskite solar cells using solution-derived NiO_x hole contacts. *ACS Nano* 10, 3630–3636. <https://doi.org/10.1021/acs.nano.5b08135>.
15. Najafi, M., Di Giacomo, F., Zhang, D., Shanmugam, S., Senes, A., Verhees, W., Hadipour, A., Galagan, Y., Aernouts, T., Veenstra, S., and Andriessen, R. (2018). Highly efficient and stable flexible perovskite solar cells with metal oxides nanoparticle charge extraction layers. *Small* 14, e1702775. <https://doi.org/10.1002/smll.201702775>.
16. Zhang, H., Cheng, J., Lin, F., He, H., Mao, J., Wong, K.S., Jen, A.K.Y., and Choy, W.C.H. (2016). Pinhole-free and surface-nanostructured NiO_x film by room-temperature solution process for high-performance flexible perovskite solar cells with good stability and reproducibility. *ACS Nano* 10, 1503–1511. <https://doi.org/10.1021/acs.nano.5b07043>.
17. Bao, H., Du, M., Wang, H., Wang, K., Zuo, X., Liu, F., Liu, L., Eder, D., Cherevan, A., Wang, S., et al. (2021). Samarium-doped nickel oxide for superior inverted perovskite solar cells: insight into doping effect for electronic applications. *Adv. Funct. Mater.* 31, 2102452. <https://doi.org/10.1002/adfm.202102452>.
18. Sahli, F., Werner, J., Kamino, B.A., Bräuninger, M., Monnard, R., Paviet-Salomon, B., Barraud, L., Ding, L., Diaz Leon, J.J., Sacchetto, D., et al. (2018). Fully textured monolithic perovskite/silicon tandem solar cells with 25.2% power conversion efficiency. *Nat. Mater.* 17, 820–826. <https://doi.org/10.1038/s41563-018-0115-4>.
19. Feng, J., Jiao, Y., Wang, H., Zhu, X., Sun, Y., Du, M., Cao, Y., Yang, D., and Liu, S. (2021). High-throughput large-area vacuum deposition for high-performance formamidinium-based perovskite solar cells. *Energy Environ. Sci.* 14, 3035–3043. <https://doi.org/10.1039/D1EE00634G>.
20. Meyer, J., Hamwi, S., Kröger, M., Kowalsky, W., Riedl, T., and Kahn, A. (2012). Transition metal oxides for organic electronics: energetics, device physics and applications. *Adv. Mater.* 24, 5408–5427. <https://doi.org/10.1002/adma.201201630>.
21. Aydin, E., Troughton, J., De Bastiani, M., Ugur, E., Sajjad, M., Alzahrani, A., Neophytou, M., Schwingenschlögl, U., Laquai, F., Baran, D., and De Wolf, S. (2018). Room-temperature-sputtered nanocrystalline nickel oxide as hole transport layer for p–i–n perovskite solar cells. *ACS Appl. Energy Mater.* 1, 6227–6233. <https://doi.org/10.1021/acsasem.8b01263>.
22. Zheng, X., Song, Z., Chen, Z., Bista, S.S., Gui, P., Shrestha, N., Chen, C., Li, C., Yin, X., Awni, R.A., et al. (2020). Interface modification of sputtered NiO_x as the hole-transporting layer for efficient inverted planar perovskite solar cells. *J. Mater. Chem. C* 8, 1972–1980. <https://doi.org/10.1039/C9TC05759E>.
23. Zhumagali, S., Isikgor, F.H., Maity, P., Yin, J., Ugur, E., De Bastiani, M., Subbiah, A.S., Mirabelli, A.J., Azmi, R., Harrison, G.T., et al. (2021). Linked nickel oxide/perovskite interface passivation for high-performance textured monolithic tandem solar cells. *Adv. Energy Mater.* 11, 2101662. <https://doi.org/10.1002/aenm.202101662>.
24. Li, G., Jiang, Y., Deng, S., Tam, A., Xu, P., Wong, M., and Kwok, H.S. (2017). Overcoming the limitations of sputtered nickel oxide for high-efficiency and large-area perovskite solar cells. *Adv. Sci.* 4, 1700463. <https://doi.org/10.1002/advs.201700463>.
25. Agarwal, D.C., Chauhan, R.S., Kumar, A., Kabiraj, D., Singh, F., Khan, S.A., Avasthi, D.K., Pivin, J.C., Kumar, M., Ghatak, J., and Satyam, P.V. (2006). Synthesis and characterization of ZnO thin film grown by electron beam evaporation. *J. Appl. Phys.* 99, 123105.
26. Pae, S.R., Byun, S., Kim, J., Kim, M., Gereige, I., and Shin, B. (2018). Improving uniformity and reproducibility of hybrid perovskite solar cells via a low-temperature vacuum deposition process for NiO_x hole transport layers. *ACS Appl. Mater. Interfaces* 10, 534–540. <https://doi.org/10.1021/acsami.7b14499>.
27. Routledge, T.J., Wong-Stringer, M., Game, O.S., Smith, J.A., Bishop, J.E., Vaenas, N., Freestone, B.G., Coles, D.M., McArdle, T., Buckley, A.R., and Lidzey, D.G. (2019). Low-temperature, high-speed reactive deposition of metal oxides for perovskite solar cells. *J. Mater. Chem. A* 7, 2283–2290. <https://doi.org/10.1039/C8TA10827G>.
28. Pang, S., Zhang, C., Dong, H., Chen, D., Zhu, W., Xi, H., Chang, J., Lin, Z., Zhang, J., and Hao, Y. (2019). Efficient NiO_x hole transporting layer obtained by the oxidation of metal nickel film for perovskite solar cells. *ACS Appl. Energy Mater.* 2, 4700–4707. <https://doi.org/10.1021/acsasem.9b00169>.
29. Abzieher, T., Moghadamzadeh, S., Schackmar, F., Eggers, H., Sutterlüt, F., Farooq, A., Kojda, D., Habicht, K., Schmager, R., Mertens, A., et al. (2019). Electron-beam-evaporated nickel oxide hole transport layers for perovskite-based photovoltaics. *Adv. Energy Mater.* 9, 1802995. <https://doi.org/10.1002/aenm.201802995>.
30. Eggers, H., Schackmar, F., Abzieher, T., Sun, Q., Lemmer, U., Vaynzof, Y., Richards, B.S., Hernandez-Sosa, G., and Paetzold, U.W. (2020). Inkjet-printed micrometer-thick perovskite solar cells with large columnar grains. *Adv. Energy Mater.* 10, 1903184. <https://doi.org/10.1002/aenm.201903184>.
31. Hossain, M., Zakaria, Y., Zikri, A., Samara, A., Aissa, B., El-Mellouhi, F., Hasan, N., Belaidi, A., Mahmood, A., and Mansour, S. (2020). E-beam evaporated hydrophobic metal oxide thin films as carrier transport materials for large scale perovskite solar cells. *Mater. Technol.* 37, 248–259.

32. Nishihara, Y., Chikamatsu, M., Kazaoui, S., Miyadera, T., and Yoshida, Y. (2018). Influence of O₂ plasma treatment on NiO_x layer in perovskite solar cells. *Jpn. J. Appl. Phys.* 57, 04FS07. <https://doi.org/10.7567/JJAP.57.04FS07>.
33. Islam, R., Chen, G., Ramesh, P., Suh, J., Fuchigami, N., Lee, D., Littau, K.A., Weiner, K., Collins, R.T., and Saraswat, K.C. (2017). Investigation of the changes in electronic properties of nickel oxide (NiO_x) due to UV/ozone treatment. *ACS Appl. Mater. Interfaces* 9, 17201–17207. <https://doi.org/10.1021/acsami.7b01629>.
34. Ratcliff, E.L., Meyer, J., Steirer, K.X., Garcia, A., Berry, J.J., Ginley, D.S., Olson, D.C., Kahn, A., and Armstrong, N.R. (2011). Evidence for near-surface NiOOH species in solution-processed NiO_x selective interlayer materials: impact on energetics and the performance of polymer bulk heterojunction photovoltaics. *Chem. Mater.* 23, 4988–5000. <https://doi.org/10.1021/cm202296p>.
35. Beverskog, B., and Puigdomenech, I. (1997). Revised Pourbaix diagrams for nickel at 25–300°C. *Corros. Sci.* 39, 969–980.
36. Boyd, C.C., Shallcross, R.C., Moot, T., Kerner, R., Bertoluzzi, L., Onno, A., Kavadiya, S., Chosy, C., Wolf, E.J., Werner, J., et al. (2020). Overcoming redox reactions at perovskite-nickel oxide interfaces to boost voltages in perovskite solar cells. *Joule* 4, 1759–1775. <https://doi.org/10.1016/j.joule.2020.06.004>.
37. Di Girolamo, D., Matteocci, F., Kosasih, F.U., Chistiakova, G., Zuo, W., Divitini, G., Korte, L., Ducati, C., Di Carlo, A., Dini, D., and Abate, A. (2019). Stability and dark hysteresis correlate in NiO-based perovskite solar cells. *Adv. Energy Mater.* 9, 1901642. <https://doi.org/10.1002/aenm.201901642>.
38. Wang, Y., Ju, H., Mahmoudi, T., Liu, C., Zhang, C., Wu, S., Yang, Y., Wang, Z., Hu, J., Cao, Y., et al. (2021). Cation-size mismatch and interface stabilization for efficient NiO_x-based inverted perovskite solar cells with 21.9% efficiency. *Nano Energy* 88, 106285. <https://doi.org/10.1016/j.nanoen.2021.106285>.
39. Chen, W., Zhu, Y., Xiu, J., Chen, G., Liang, H., Liu, S., Xue, H., Birgersson, E., Ho, J.W., Qin, X., et al. (2022). Monolithic perovskite/organic tandem solar cells with 23.6% efficiency enabled by reduced voltage losses and optimized interconnecting layer. *Nat. Energy* 7, 229–237. <https://doi.org/10.1038/s41560-021-00966-8>.
40. Chen, W., Zhou, Y., Wang, L., Wu, Y., Tu, B., Yu, B., Liu, F., Tam, H.W., Wang, G., Djurišić, A.B., et al. (2018). Molecule-doped nickel oxide: verified charge transfer and planar inverted mixed cation perovskite solar cell. *Adv. Mater.* 30, e1800515. <https://doi.org/10.1002/adma.201800515>.
41. Ru, P., Bi, E., Zhang, Y., Wang, Y., Kong, W., Sha, Y., Tang, W., Zhang, P., Wu, Y., Chen, W., et al. (2020). High electron affinity enables fast hole extraction for efficient flexible inverted perovskite solar cells. *Adv. Energy Mater.* 10, 1903487. <https://doi.org/10.1002/aenm.201903487>.
42. Liu, Z., Qiu, L., Ono, L.K., He, S., Hu, Z., Jiang, M., Tong, G., Wu, Z., Jiang, Y., Son, D.-Y., et al. (2020). A holistic approach to interface stabilization for efficient perovskite solar modules with over 2,000-hour operational stability. *Nat. Energy* 5, 596–604. <https://doi.org/10.1038/s41560-020-0653-2>.
43. Werner, J., Geissbühler, J., Dabirian, A., Nicolay, S., Morales-Masis, M., Wolf, S.D., Niesen, B., and Ballif, C. (2016). Parasitic absorption reduction in metal oxide-based transparent electrodes: application in perovskite solar cells. *ACS Appl. Mater. Interfaces* 8, 17260–17267. <https://doi.org/10.1021/acsami.6b04425>.
44. Hu, K., Wang, F., Liu, H., Li, Y., and Zeng, W. (2020). Enhanced hydrogen gas sensing properties of Pd-doped SnO₂ nanofibres by Ar plasma treatment. *Ceram. Int.* 46, 1609–1614. <https://doi.org/10.1016/j.ceramint.2019.09.132>.
45. Edelberg, E.A., Perry, A., Benjamin, N., and Aydi, E.S. (1999). Energy distribution of ions bombarding biased electrodes in high density plasma reactors. *J. Vac. Sci. Technol. A* 17, 506–516. <https://doi.org/10.1116/1.581612>.
46. Luo, D., Yang, W., Wang, Z., Sadhanala, A., Hu, Q., Su, R., Shivanna, R., Trindade, G.F., Watts, J.F., Xu, Z., et al. (2018). Enhanced photovoltage for inverted planar heterojunction perovskite solar cells. *Science* 360, 1442–1446. <https://doi.org/10.1126/science.aap9282>.
47. Hu, Q., Chen, W., Yang, W., Li, Y., Zhou, Y., Larson, B.W., Johnson, J.C., Lu, Y.-H., Zhong, W., Xu, J., et al. (2020). Improving efficiency and stability of perovskite solar cells enabled by a near-infrared-absorbing moisture barrier. *Joule* 4, 1575–1593. <https://doi.org/10.1016/j.joule.2020.06.007>.
48. Chen, C., Liang, J., Zhang, J., Liu, X., Yin, X., Cui, H., Wang, H., Wang, C., Li, Z., Gong, J., et al. (2021). Interfacial engineering of a thiophene-based 2D/3D perovskite heterojunction for efficient and stable inverted wide-bandgap perovskite solar cells. *Nano Energy* 90, 106608. <https://doi.org/10.1016/j.nanoen.2021.106608>.
49. Yang, G., Ren, Z., Liu, K., Qin, M., Deng, W., Zhang, H., Wang, H., Liang, J., Ye, F., Liang, Q., et al. (2021). Stable and low-photovoltage-loss perovskite solar cells by multifunctional passivation. *Nat. Photon.* 15, 681–689. <https://doi.org/10.1038/s41566-021-00829-4>.
50. Wang, M., Zhao, Y., Jiang, X., Yin, Y., Yavuz, I., Zhu, P., Zhang, A., Han, G.S., Jung, H.S., Zhou, Y., et al. (2022). Rational selection of the polymeric structure for interface engineering of perovskite solar cells. *Joule* 6, 1032–1048. <https://doi.org/10.1016/j.joule.2022.04.002>.
51. Wu, S., Zhang, J., Li, Z., Liu, D., Qin, M., Cheung, S.H., Lu, X., Lei, D., So, S.K., Zhu, Z., and Jen, A.K.-Y. (2020). Modulation of defects and interfaces through alkylammonium interlayer for efficient inverted perovskite solar cells. *Joule* 4, 1248–1262. <https://doi.org/10.1016/j.joule.2020.04.001>.
52. Chen, W., Zhou, Y., Chen, G., Wu, Y., Tu, B., Liu, F.-Z., Huang, L., Ng, A.M.C., Djurišić, A.B., and He, Z. (2019). Alkali chlorides for the suppression of the interfacial recombination in inverted planar perovskite solar cells. *Adv. Energy Mater.* 9, 1803872. <https://doi.org/10.1002/aenm.201803872>.
53. Zheng, X., Troughton, J., Gasparini, N., Lin, Y., Wei, M., Hou, Y., Liu, J., Song, K., Chen, Z., Yang, C., et al. (2019). Quantum dots supply bulk- and surface-passivation agents for efficient and stable perovskite solar cells. *Joule* 3, 1963–1976. <https://doi.org/10.1016/j.joule.2019.05.005>.
54. Yang, D., Yang, R., Wang, K., Wu, C., Zhu, X., Feng, J., Ren, X., Fang, G., Priya, S., and Liu, S.F. (2018). High efficiency planar-type perovskite solar cells with negligible hysteresis using EDTA-complexed SnO₂. *Nat. Commun.* 9, 3239. <https://doi.org/10.1038/s41467-018-05760-x>.
55. Guerrero, A., Garcia-Belmonte, G., Mora-Sero, I., Bisquert, J., Kang, Y.S., Jacobsson, T.J., Correa-Baena, J.-P., and Hagfeldt, A. (2016). Properties of contact and bulk impedances in hybrid lead halide perovskite solar cells including inductive loop elements. *J. Phys. Chem. C* 120, 8023–8032. <https://doi.org/10.1021/acs.jpcc.6b01728>.
56. Zarazua, I., Han, G., Boix, P.P., Mhaisalkar, S., Fabregat-Santiago, F., Mora-Seró, I., Bisquert, J., and Garcia-Belmonte, G. (2016). Surface recombination and collection efficiency in perovskite solar cells from impedance analysis. *J. Phys. Chem. Lett.* 7, 5105–5113. <https://doi.org/10.1021/acs.jpclett.6b02193>.
57. Pascoe, A.R., Duffy, N.W., Scully, A.D., Huang, F., and Cheng, Y.-B. (2015). Insights into planar CH₃NH₃PbI₃ perovskite solar cells using impedance spectroscopy. *J. Phys. Chem. C* 119, 4444–4453. <https://doi.org/10.1021/jp509896u>.
58. Mihailitchi, V.D., Wildeman, J., and Blom, P.W. (2005). Space-charge limited photocurrent. *Phys. Rev. Lett.* 94, 126602. <https://doi.org/10.1103/PhysRevLett.94.126602>.
59. Yang, D., Zhou, X., Yang, R., Yang, Z., Yu, W., Wang, X., Li, C., Liu, S.F., and Chang, R.P.H. (2016). Surface optimization to eliminate hysteresis for record efficiency planar perovskite solar cells. *Energy Environ. Sci.* 9, 3071–3078.

Joule, Volume 6

Supplemental information

Surface redox engineering of vacuum-deposited NiO_x for top-performance perovskite solar cells and modules

Minyong Du, Shuai Zhao, Lianjie Duan, Yuexian Cao, Hui Wang, Youming Sun, Likun Wang, Xuejie Zhu, Jiangshan Feng, Lu Liu, Xiao Jiang, Qingshun Dong, Yantao Shi, Kai Wang, and Shengzhong (Frank) Liu

Supplemental Experimental Procedures

Material

Lead iodide (PbI_2 , 99.999%), Formamidinium iodide ($\text{H}_2\text{N}=\text{CHNH}_2\text{I}$; FAI), methylamine hydrochloride ($\text{CH}_3\text{NH}_3\text{Cl}$; MACl), bathocuproine (BCP) were purchased from Xi'an Polymer Light Technology. [6,6]-phenyl- C_{61} -butyric acid methyl ester (PC_{61}BM) was purchased from Advanced Election Technology CO., Ltd.. N,N-dimethylformamide (DMF, 99.8%), N-Methyl-2-Pyrrolidinone (NMP, 99.5%), dimethyl sulfoxide (DMSO, 99.9%), isopropanol (99.9%), L- α -phosphatidylcholine, ionic liquid BMIMBF₄ and nickel peroxide (NiO_2) were purchased from Sigma-Aldrich. Chlorobenzene (CB), acetic acid and phosphoric acid were purchased from Sinopharm Chemical Reagent Co., Ltd. HNO_3 solution (65-68%) was purchased from Tianjin Kemiou Chemical Reagent Co., Ltd.. Nickel oxide (99.99%, diameter around 3mm) was purchased from Zhong Nuo Advanced Material (Beijing) Technology Co., Ltd.. Ni_2O_3 was purchased from Macklin. Others materials were purchased from Alfa Aesar. All the salts and solvents were used as received without any further purification.

Devices fabrication

MgF₂/PET/ITO Substrate Preparation:

For flexible substrate, ~ 90 nm MgF₂ film was deposited on the front surface of PET by using electron beam evaporation as an antireflection layer.¹ ITO layers were deposited by using radio frequency (RF, 13.56 MHz) magnetron sputtering from ITO target ($\text{In}_2\text{O}_3:\text{SnO}_2 = 90:10$, 99.99% purity) at room temperature. The base pressure for deposition was $< 6.7 \times 10^{-4}$ Pa. Before deposition, the target was pre-sputtered for 5 min to remove the contamination layer. The optimized deposition parameters of ITO layers are listed in **Table S1**.

Preparation of NiO_x films:

The FTO glass or MgF₂/PET/ITO substrates were cleaned by using acetone and isopropanol in an ultrasonic bath for 30 min. After that, the substrates were transferred into an electron beam evaporation system. Before evaporation, the base pressure of the system was $\sim 7 \times 10^{-4}$ Pa. During the evaporation, a small flow of oxygen in the range of 15 sccm was present to improve the composition of the NiO_x films, and the substrates were kept at room temperature in the whole process, the thickness of the NiO_x was monitored by the crystal oscillator, and the thickness was set 26 nm.

SRE for the EBE-NiO_x films:

Ar plasma treatments were carried out in a vacuum plasma cleaning system with 13.65 MHz RF power supply. The base pressure was pumped to ~ 1 Pa. Subsequently, the chamber was flooded with 23 sccm argon to a pressure of approximately 21 Pa, then the substrates were treated at a plasma power of 30 W for 2.5 min. After that, we use the dilute nitric acid (~0.015 M) to treated the NiO_x-based substrates. Here, the small-area substrates were treated by spin-coating at a rate of 5000 rpm for 35 s. The large-area substrates were soaked in dilute nitric acid for 3s and dried with nitrogen.

Preparation of small area PSCs

The perovskite precursor solution was prepared by dissolving FAI = 1.14 M, PbI_2 = 1.33 M, CsI = 0.1 M and MACl = 0.2 M in mixed solvent (DMF:DMSO = 4:1) with additives of L- α -Phosphatidylcholine (0.06 mg/ml) and ionic liquid BMIMBF₄ (0.33 mg/ml).^{2,3} For rigid devices, the perovskite film was prepared on SRE treated NiO_x -based substrates by slot-die coating at room temperature. The process parameters of slot-die coating was described in our previous report.⁴ After coating the precursor solution, the substrate was put in a vacuum chamber, which was evacuated for 39 s, and then the perovskite film was directly annealed at 110 °C for 20 min. Different with rigid devices, MgF_2 /PET/ITO flexible substrates were cut to obtain substrates with the size of $5 \times 2.5 \text{ cm}^2$ before preparing perovskite. Then the flexible substrate was placed on the vacuum adsorption platform of slot-die coating equipment, and the coating process was same as that of rigid devices. After finished the annealing step, the flexible substrate was cut into small pieces with the size of $2.5 \times 2.5 \text{ cm}^2$. The PC₆₁BM (20 mg/ml CB) was spin-coated at a rate of 4000 rpm for 30 s. The saturated solution of BCP in isopropanol was spin-coated at a rate of 5000 rpm for 40s. Lastly, ~80 nm Ag was evaporated on the substrates to form electrode. The active area is 0.09 cm^2 .

Preparation of large-area PSC Modules

For modules, the perovskite precursor was prepared by dissolving FAI = 1.03 M, PbI_2 = 1.21 M, CsI = 0.09 M, MACl = 0.19 M in mixed solvent (DMF:NMP = 6:1) with additive L- α -Phosphatidylcholine (0.06 mg/ml) and ionic liquid BMIMBF₄ (0.33 mg/ml). Upon slot-die coating, the substrate was quickly transferred to the vacuum chamber, which was evacuated for 40 s, and then the perovskite film was directly put into the oven of 115 °C for 20 min in atmospheric environment. Details of the process for the perovskite films was shown in **Video S1**. Then PC₆₁BM solution (15 mg/ml CB) and BCP saturated isopropanol solution were spin coated on perovskite films in succession at room temperature. The rotating speed and time were 1500 rpm and 30 s, respectively. The metal electrode evaporated Ag of 130 nm. To fabricate modules, the FTO electrode, NiO_x /perovskite/PC₆₁BM/BCP stacking layer, and Ag electrode were ablated by laser scribe sequentially to form a P1-P2-P3 pattern. The laser process and parameter of the module is same with our previous report.⁴ A structure sketch map of the large-area perovskite submodule is shown in **Figure S17A**, where the part between P1 and P3 (black shadow area) is the dead area, and the red shadow area is the active area. The calculation formula of the active area of the submodule is: electrode length \times width of active area \times number of subcells, and the geometrical fill factor is calculated according to the formula of (active area)/(active area + dead area). The width of the dead area is measured by using the microscope as shown in **Figure S17B**, the width of P1, P2 and P3 and the distance of adjacent lines are about 200 μm . For testing long-term stability, we replaced the Ag electrode with the combination of 20 nm Cr and 130 nm Au.³

Device characterization

For small devices, the J - V measurement was performed by using a Keysight B2901A

Source-Meter under simulated AM 1.5 G irradiation produced by a xenon-lamp-based solar simulator (Newport, Class AAA Solar Simulator). The scan rate was 0.01 V/s and the delay time was 1 ms. For large-scale modules, the I - V measurement was performed by using a Keithley 2460 Source-Meter under simulated AM 1.5 G irradiation produced by a xenon-lamp-based solar simulator (WACOM, Class AAA Solar Simulator). The scan rate was 0.1 V/s and the delay time was 1 ms. We use a silicon reference cell to calibrate the light intensity of solar simulator, which was certificated by National Institute of Metrology, China. The external quantum efficiency (EQE) spectra were obtained by using an Enlitech QE (R3018) measurement system. XRD patterns of various films were performed by using a Dandong DX-2700BH with Cu K α 1 irradiation ($\lambda=1.541$ Å). UV-vis absorption spectra were recorded by using a UV-vis spectrophotometer (UH-4150 Hitachi). The film morphologies were measured by using SEM (Hitachi SU8020). The AFM and KPFM images were obtained using an atomic force microscope (Dimension Icon, BRUKER, USA) in the contact mode according to the previous literature.⁵ The C-AFM measurement was performed by using an atomic force microscope (BRUKER, Nanowizard 4XP), where a SCM-PIT-v2 probe was used for the C-AFM detection. For the Mott-Schottky analysis, capacitance-voltage curves were measured by using an electrochemical workstation (Chi760e, Shanghai Chenhua). The XPS results were measured with a photoelectron spectrometer (Thermo Scientific ESCALAB 250Xi). The XPS spectra were calibrated on the basis of the C 1s peak at 284.5 eV. The PL was measured by using a PicoQuant FT-300 and FT-100 with a pulsed diode laser at 510 nm. The time-resolved PL curves were fitted according to the equation $Y = A_1 e^{\frac{-t}{\tau_1}} + A_2 e^{\frac{-t}{\tau_2}} + Y_0$, where A_1 and A_2 are the decay amplitudes, τ_1 and τ_2 are the decay times and Y_0 is a constant for the baseline offset. The average lifetime τ_{ave} was calculated according to the equation $\tau_{ave} = \frac{A_1 \tau_1^2 + A_2 \tau_2^2}{A_1 \tau_1 + A_2 \tau_2}$. The EIS measurements were conducted by using the electrochemical workstation (ZENNIUM, Zahner, Germany) under dark conditions. The measured frequencies ranged from 1 Hz to 1 MHz with varying bias from 0 to 0.5 V. The amplitude was 10 mV. The dark J - V of devices were measured by a Keysight B2901A Source-Meter. The scan rate was 0.003 V/s, and the range was from 0 V to 3 V. The carrier concentration and hole mobility were measured by Accent HL5500 Hall System with a magnetic field strength of 0.5 T in a van der Pauw method, the film thickness is ~ 20 nm.

Computational methods

All DFT calculations were performed with the plane-wave approach using the Quantum ESPRESSO package.⁶ The Perdew–Burke–Ernzerh of exchange-correlation functional was employed with the scalar relativistic ultrasoft pseudopotentials.⁷ The cutoff of plane-wave basis was set to 40 and 320 Ry for the wave function and augmented density, respectively. The DFT+ U method ($U = 4$ eV for Ni 3d state) was applied to eliminate the self-interaction error resulting from the intra-atomic exchange interaction of the localized d -electrons.⁸ The lattice parameters were relaxed with the force convergence threshold of 10^{-3} Ry/Bohr. To investigate the defect properties of

NiO, a 128-atom supercell with a $2 \times 2 \times 2$ k -mesh grid was used to calculate the formation energies (E_f) of Ni and O vacancies according to $E_f = E_d - E_p + \sum_i n_i \mu_i + qE_F + E_{\text{corr}}$, where E_d and E_p are total energies of NiO supercells with and without vacancy, respectively. n_i is the number of atoms removed from the supercell. μ_i is the reservoir chemical potential of the defect atom. q and E_F represent the charge state of defect and the Fermi level. The last term E_{corr} is a correction for the long-range Coulomb interaction of charged defects under the periodic boundary condition.⁹ To study the effect of the NO_3 on the electronic properties, the $2 \times 2 \times 3$ NiO supercell was created by adding a 20 Å of vacuum along the c -direction. The surface structure was relaxed with a $4 \times 4 \times 1$ k -mesh grid, and atoms of bottom two layers were fixed during the atomic position relaxation.

To investigate the influence of HNO_3 treatment on the electronic properties of NiO layer, we firstly calculated the adsorption energy E_{ads} of NO_3^- on the NiO surface according to $E_{\text{ads}} = E(\text{NiO-NO}_3) - E(\text{NiO}) + E(\text{NO}_3)$, where $E(\text{NiO-NO}_3)$, $E(\text{NiO})$ and $E(\text{NO}_3)$ are energies of NiO surface adsorbed NO_3^- , the NiO surface and the NO_3^- molecular, respectively. To elucidate the charge transfer between the NiO with NO_3^- group, the charge density difference was calculated by $\Delta\rho = \rho(\text{NiO}) + \rho(\text{NO}_3) - \rho(\text{NiO-NO}_3)$, where $\rho(\text{NO}_3)$, $\rho(\text{NiO})$ and $\rho(\text{NiO-NO}_3)$ are the charge densities of the NO_3^- molecule, the surface structures without and with NO_3^- adsorption, respectively.

Device stability testing

The PSCs were simply encapsulated with a cover glass and UV adhesive (NOA81, Norland) in atmospheric environment. The non-encapsulated devices were aged in a desiccator (humidity < 20%) at room temperature (~25 °C). For light-soaking stability testing, the unencapsulated PSCs were placed in a glove box under a N_2 atmosphere. The PSCs were biased at the maximum power-point voltage using a potentiostat under continuous one-sun-intensity white-LED illumination at around 45 °C.¹⁰

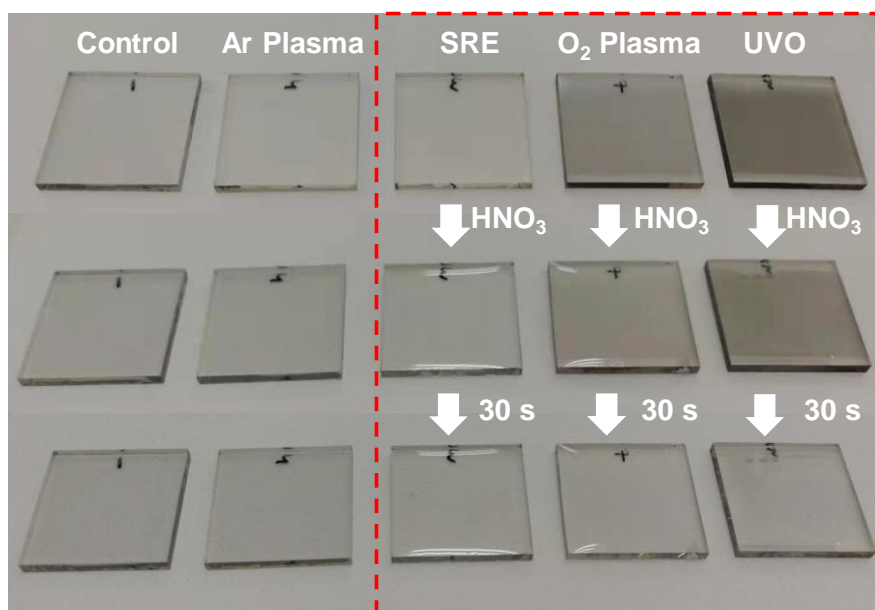


Figure S1. Photograph of various treated NiO_x films before and after HNO_3 treatment. From left to right: control, treated with Ar plasma, SRE, O_2 plasma and UVO.

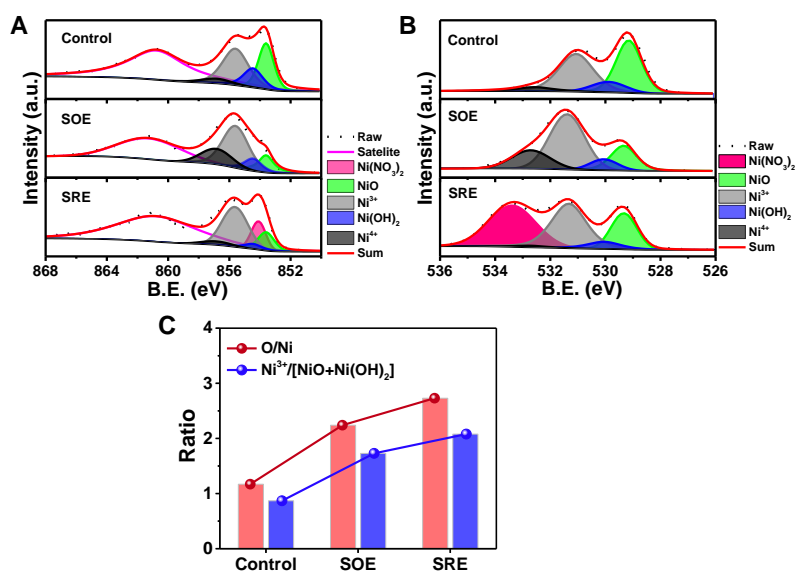


Figure S2. XPS spectra and analysis of control, SOE and SRE NiO_x films. (A) Ni 2p_{3/2} core level spectra, (B) O 1s core level spectra, (C) the O/Ni and $\text{Ni}^{3+}/\text{Ni}^{2+}$ ratio.

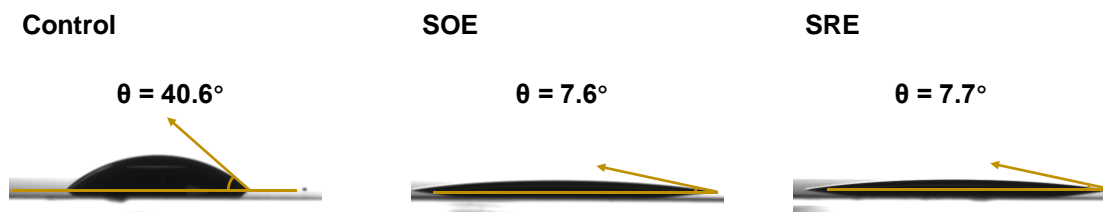


Figure S3. The contact angle measurement of a water droplet on control, SOE and SRE treated NiO_x films.

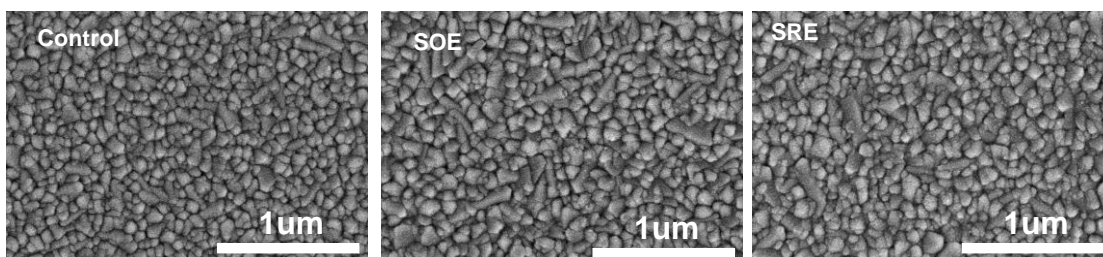


Figure S4. Top view SEM images of control, SOE and SRE treated NiO_x films.

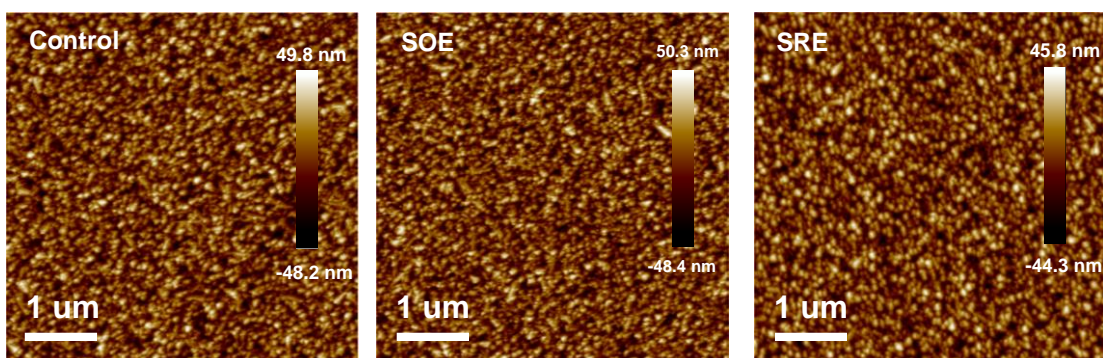


Figure S5. The AFM images of control, SOE and SRE treated NiO_x films.

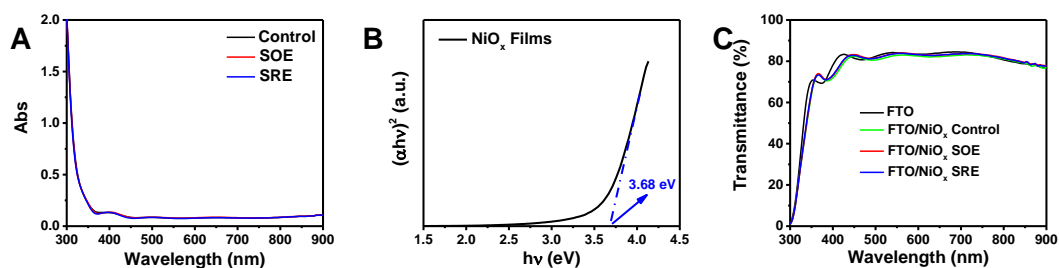


Figure S6. The optical properties of NiO_x films. (A) UV-vis absorption spectra of control, SOE and SRE NiO_x films/FTO glass. (B) The optical band gap of NiO_x films. (C) UV-vis transmittance spectra of FTO glass and control, SOE treated, SRE treated FTO/ NiO_x films.

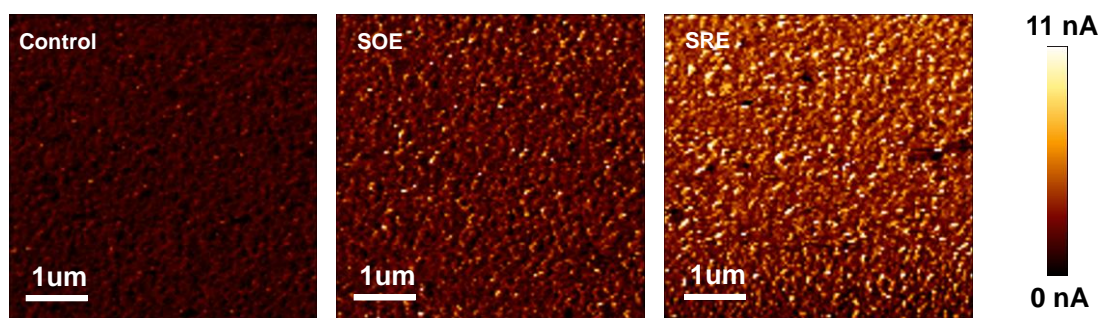


Figure S7. The C-AFM maps of control, SOE and SRE treated NiO_x films.

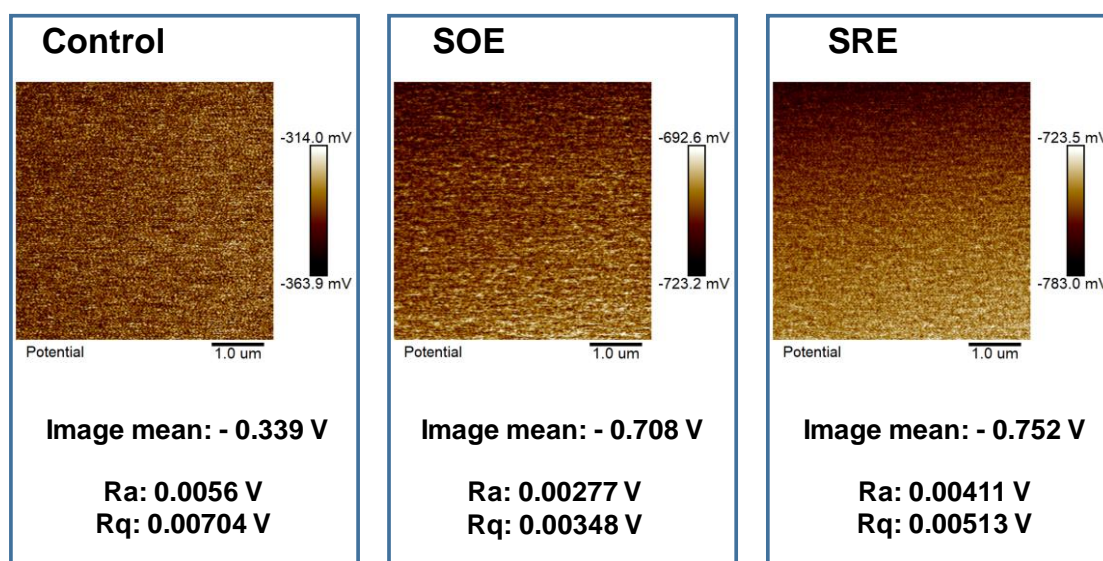


Figure S8. The KPFM maps of control, SOE and SRE treated NiO_x films.

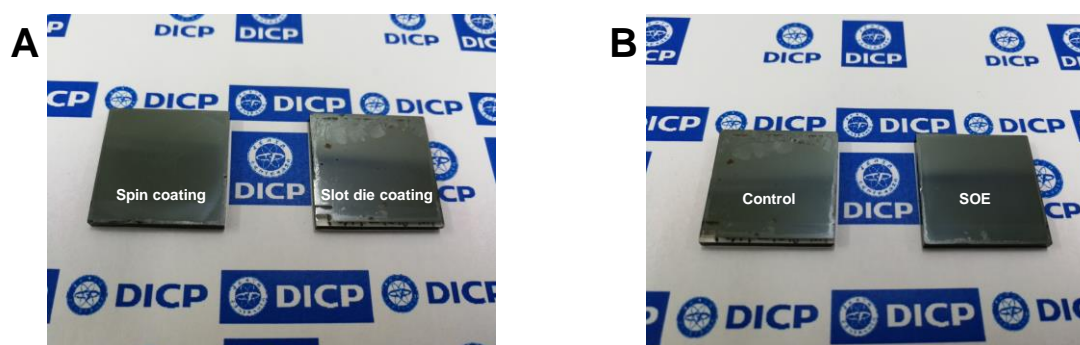


Figure S9. Photographs of perovskite films coated on different NiO_x films via different technologies. (A) Spin coating and slot die coating without Ar plasma treatment. (B) Perovskite films fabricated on NiO_x film with and without Ar plasma treatment by slot die coating.

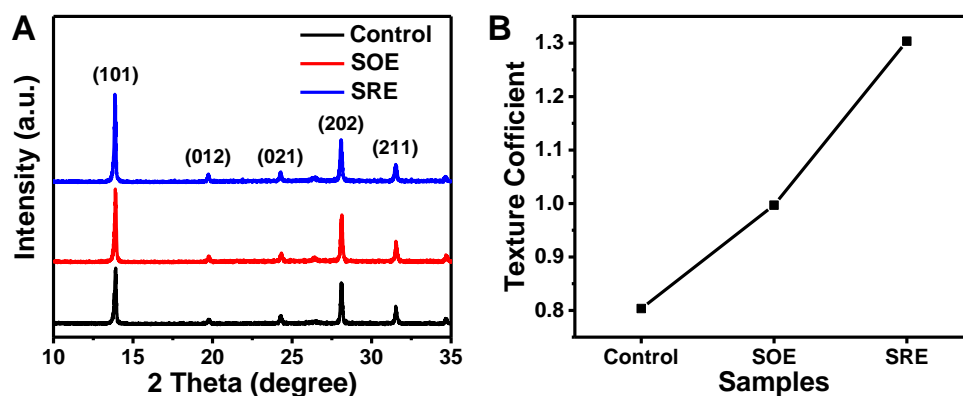


Figure S10. Crystallization of the perovskite films on control, SOE and SRE treated NiO_x films. (A) The XRD diffractograms. (B) The texture coefficient of (101) plane.

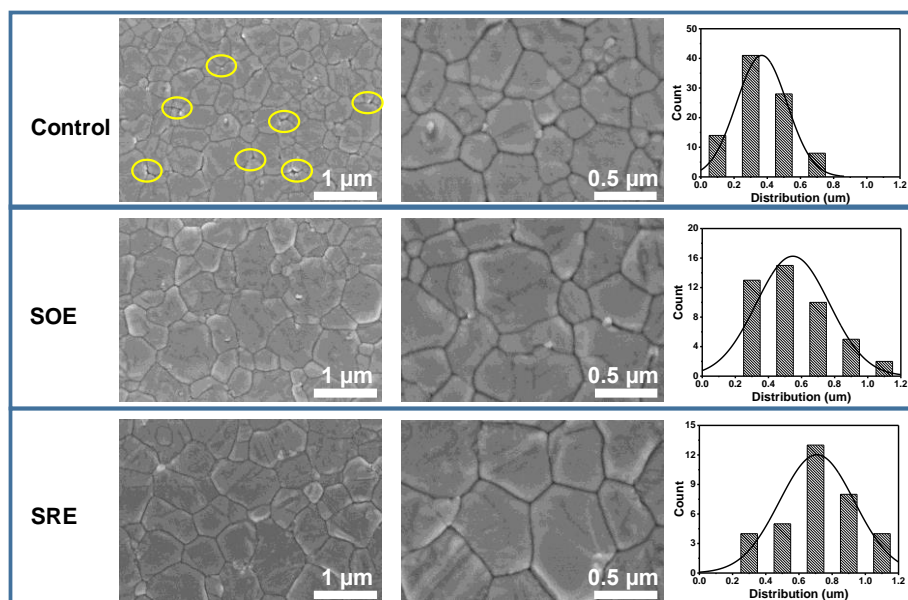


Figure S11. The top-view SEM images of perovskite films fabricated on the control, SOE and SRE treated NiO_x films. Right is the column chart of corresponding grain sizes counted by the SEM images.

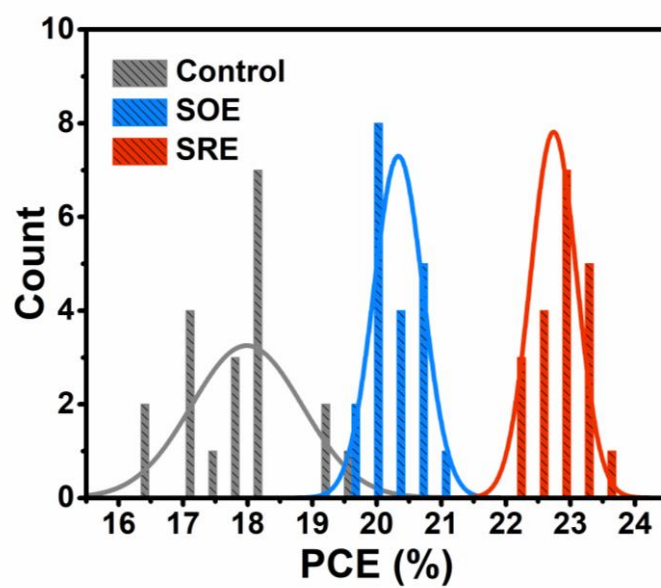


Figure S12. The PCE distribution histogram of the PSCs fabricated on control, SOE, SRE NiO_x films, 20 cells per type (reverse scan).

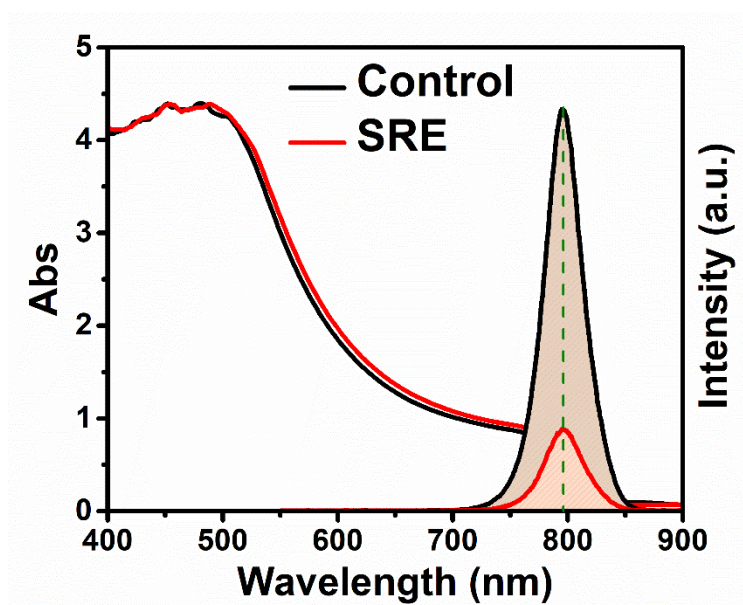


Figure S13. UV-vis absorption and normalized PL spectra of perovskite film fabricated on control and SRE treated NiO_x film.

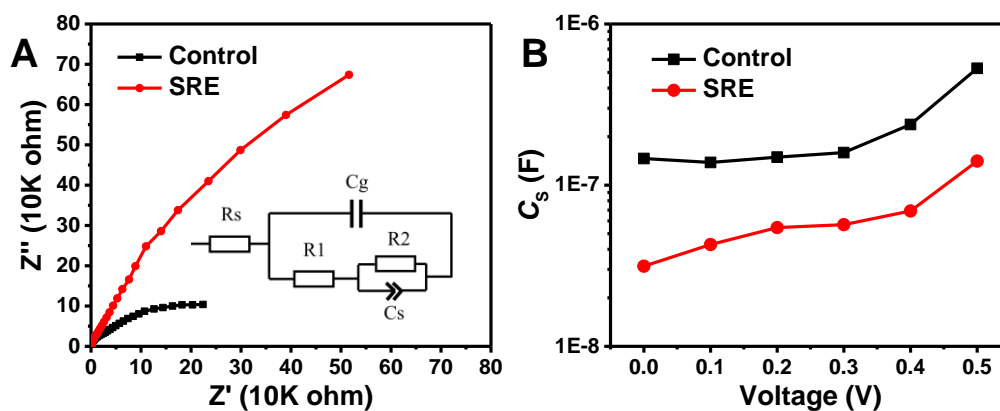


Figure S14. Electrochemical impedance spectroscopy (EIS) measurements of control and SRE-devices. (A) Nyquist plots of PSCs with and without SRE treatment under a bias voltage of 0 V. (B) C_s as a function of the bias-voltage of PSCs with and without SRE treatment.

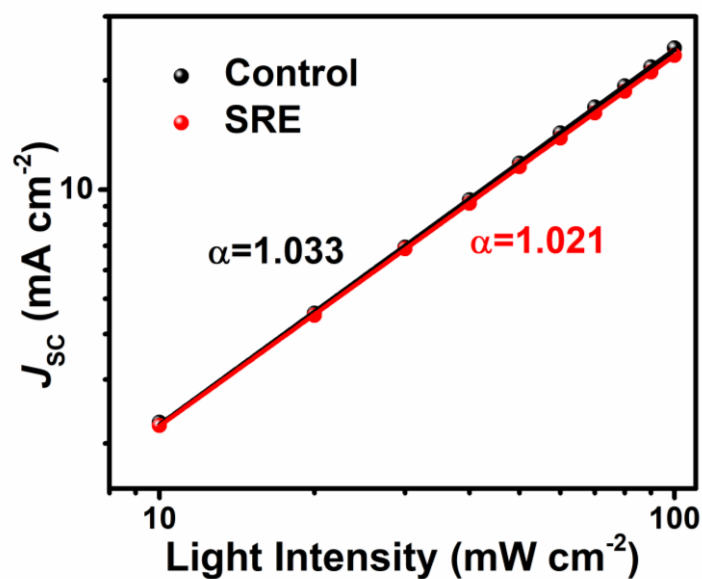


Figure S15. J_{sc} vs. light intensity curves for the PSCs fabricated on the control and SRE NiO_x films.

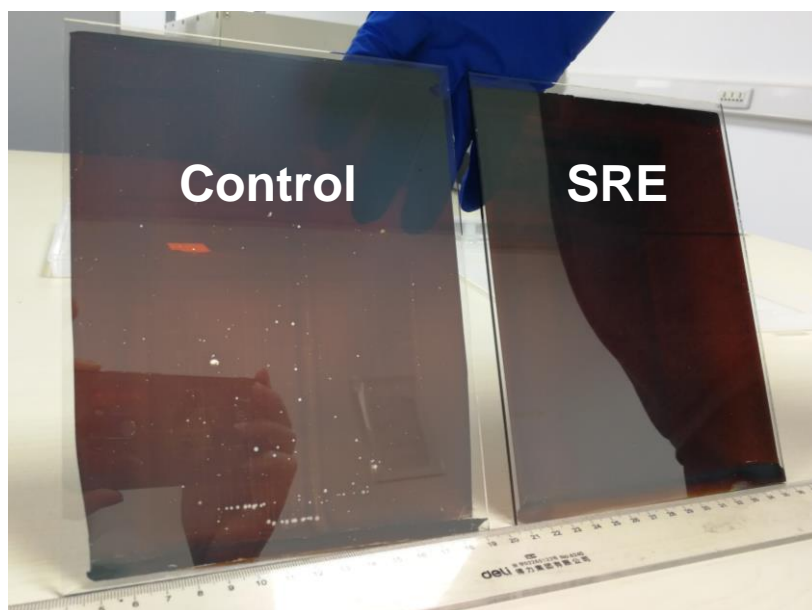


Figure S16. The photograph of the perovskite films coated on control and SRE NiO_x films ($156 \times 200 \text{ mm}^2$).

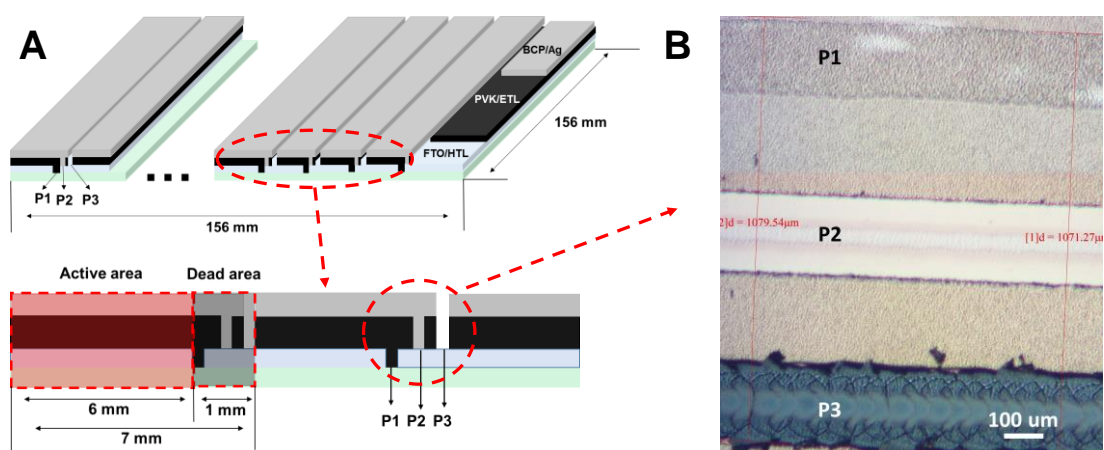


Figure S17. The calculation of the effective area of the submodule. (A) An illustration of the structure of the PSC module with a GFF of 85.7%. (B) In situ microscopy observation images of the interconnections of P1, P2 and P3.

Table S1. The process parameters of sputter ITO layers on PET substrates.

Parameters	Values
Base Pressure	6.7*10 ⁻⁴ Pa
Deposition Pressure	0.4 Pa
Power	200 W
Argon gas Flow Rate	20 sccm
Substrate Temperature	25
Rotating speed	0.25 RPM

Table S2. Peak fitting parameters of the Ni 2p_{3/2} core level spectra, include binding energies and relative composition of various nickel oxidation species.

	Sample	NiO	Ni(OH) ₂	Ni ³⁺	Ni ⁴⁺	Ni(NO ₃) ₂
BE (eV)	Control	853.6	854.45	855.6	856.85	-
	SOE	853.6	854.45	855.6	856.85	-
	SRE	853.6	854.45	855.6	856.85	854.1
Relative Composition	Control	31.5%	18.1%	43.1%	7.3%	-
	SOE	17.0%	12.1%	50.3%	20.6%	-
	SRE	16.8%	7.3%	50.1%	5.8%	20.0%

Table S3. Peak fitting parameters of the O 1s core level spectra, include binding energies and relative composition of various nickel oxidation species.

	Sample	NiO	Ni(OH) ₂	Ni ³⁺	Ni ⁴⁺	Ni(NO ₃) ₂
BE (eV)	Control	529.15	529.9	531.06	532.56	-
	SOE	529.3	530.05	531.3	532.7	-
	SRE	529.3	530.05	531.38	532.7	533.37
Relative Composition	Control	40.7%	10.8%	41.7%	6.8%	-
	SOE	20.0%	8.8%	51.5%	19.7%	-
	SRE	18.0%	6.6%	35.4%	2.1%	37.9%

Table S4. Photovoltaic parameters of the NiO_x-based PSCs fabricated on control, SOE, SRE treated NiO_x films by slot die coating.

Name	V_{oc}	J_{sc}	FF	PCE	
	(V)	(mA/cm ²)	(%)	(%)	
Control	1.01	24.2	79.9	19.6	Champion
	1.01±0.01	23.7±0.2	75.4±2.8	18.0±0.9	Average
SOE	1.10	24.3	79.6	21.2	Champion
	1.09±0.01	23.8±0.3	78.5±1.7	20.3±0.4	Average
SRE	1.16	24.8	81.4	23.4	Champion
	1.13±0.01	24.4±0.2	82.1±0.7	22.7±0.4	Average

Table S5. Photovoltaic parameters of the champion NiO_x-based PSCs with SRE treatment.

Number	V_{oc} (V)	J_{sc} (mA/cm ²)	FF (%)	PCE (%)
1	1.14	24.4	83.0	23.0
2	1.14	24.4	81.7	22.7
3	1.14	24.5	81.6	22.8
4	1.14	24.3	81.6	22.6
5	1.13	24.1	82.9	22.5
6	1.12	24.4	82.8	22.7
7	1.14	24.5	82.3	23.1
8	1.13	24.2	81.4	22.3
9	1.13	24.5	81.8	22.7
10	1.13	24.2	81.7	22.3
11	1.13	24.0	81.9	22.3
12	1.14	24.7	82.5	23.2
13	1.13	24.5	82.1	22.7
14	1.14	24.7	82.6	23.3
15	1.12	24.4	84.1	23.0
16	1.16	24.8	81.4	23.4
17	1.15	24.6	80.9	22.8
18	1.13	24.7	82.3	22.9
19	1.13	24.2	81.4	22.2
20	1.12	24.2	82.2	22.3
Average	1.13±0.01	24.4±0.2	82.1±0.7	22.7±0.4

Table S6. Photovoltaic parameters of the champion NiO_x-based flexible PSCs with SRE treatment.

Number	V_{oc} (V)	J_{sc} (mA/cm²)	FF (%)	PCE (%)
1	1.10	24.6	77.8	21.0
2	1.10	24.0	78.7	20.8
3	1.09	24.2	79.4	21.0
4	1.09	24.5	79.7	21.3
5	1.10	23.8	78.1	20.5
6	1.10	24.0	78.3	20.7
7	1.09	23.6	79.6	20.5
8	1.08	23.6	79.6	20.3
9	1.08	24.4	79.2	20.9
10	1.09	23.9	80.1	20.8
11	1.08	24.1	80.8	21.0
12	1.09	24.2	78.7	20.8
13	1.08	24.4	79.9	20.9
14	1.09	24.0	78.3	20.4
15	1.10	24.0	78.1	20.6
16	1.10	24.0	78.4	20.6
17	1.09	24.2	80.0	21.0
18	1.10	23.7	80.3	20.8
19	1.09	24.1	77.8	20.4
20	1.09	24.4	77.3	20.6
Average	1.09±0.01	24.1±0.3	79±1.0	20.8±0.3

Table S7. The PCE of the NiO_x-PSCs with various fabricated methods from other report.

Fabrication of NiO _x films	Fabrication of perovskite films	PCE (%)	Year	Ref.
Electron Beam Evaporation	Slot die coating	23.4	2022	This Work
Magnetron Sputtering	Spin-coating	9.84	2014	11
Magnetron Sputtering	Spin-coating	11.6	2014	12
Pulsed Laser Deposition	Spin-coating	17.3	2015	13
Spraying coating	Spin-coating	16.2	2015	14
Electron Beam Evaporation	Spin-coating	10.24	2016	15
Electrochemical deposition	Spin coating	19.2	2017	16
Magnetron Sputtering	Spin-coating	18.5	2017	17
Spray pyrolysis method	Spin coating	19.19	2017	18
Spray coating +chemical bath deposition	Spin coating	16.7	2018	19
Atomic layer deposition	Spin coating	18.45	2018	20
Magnetron Sputtering	Spin-coating	17.6	2018	21
Chemical bath deposition	Spin-coating	19.1	2018	22
Electron Beam Evaporation	Inkjet Printing	20.7	2019	23
Magnetron Sputtering	Spin-coating	~20	2020	24
Electron Beam Evaporation	Inkjet Printing	21.6	2020	25
Magnetron Sputtering	Spin-coating	20.4	2021	26
Blade coating	Blade coating	20.91	2021	27

Table S8. The fitted parameters of perovskite films deposited on FTO glass, control and SRE NiO_x films substrates from TRPL spectra.

Sample	τ_{ave} (ns)	τ_1 (ns)	τ_2 (ns)	A ₁	A ₂
Glass/FTO/Perovskite films	944	27.2	1011	1542.2	4158.0
Glass/FTO/NiO _x /Perovskite films	360	149.2	403.2	2256.3	4033.2
Glass/FTO/NiO _x /SRE/Perovskite films	135	101.5	164.8	5787.8	3942.6

Table S9. Photovoltaic parameters of the submodules (156*156 mm²) fabricated on SRE treated E-beam NiO_x films.

Number	<i>V</i>_{oc} (V)	<i>I</i>_{sc} (mA)	FF (%)	PCE (%)	Sub-cell size (cm²)	Number of Sub-cells	Active-area (cm²)
1	19.79	201.1	75.5	17.1	14.6*0.6	20	175.2
2	20.74	198.9	78.4	18.6	14.5*0.6	20	174.0
3	20.09	204.5	78.3	18.4	14.6*0.6	20	175.2
4	20.38	205.6	75.7	18.0	14.7*0.6	20	176.4
5	20.12	204.7	75.9	17.7	14.7*0.6	20	176.4
6	19.98	197.3	75.8	17.2	14.5*0.6	20	174.0
7	20.77	192.7	76.8	17.6	14.5*0.6	20	174.0
8	19.76	197.6	75.6	17.0	14.5*0.6	20	174.0
9	20.58	205.4	73.3	17.8	14.5*0.6	20	174.0
10	21.89	210.4	65.0	17.1	14.6*0.6	20	175.2
11	20.17	201.1	74.7	17.3	14.6*0.6	20	175.2
12	20.09	198.6	72.7	16.7	14.5*0.6	20	174
13	20.29	203.7	76.6	17.6	14.55*0.62	20	180.4
14	20.95	202.9	74.9	18.2	14.6*0.6	20	175.2

Supplemental References

1. Feng, J., Zhu, X., Yang, Z., Zhang, X., Niu, J., Wang, Z., Zuo, S., Priya, S., Liu, S., and Yang, D. (2018). Record Efficiency Stable Flexible Perovskite Solar Cell Using Effective Additive Assistant Strategy. *Adv. Mater.* *30*, 1801418. <https://doi.org/10.1002/adma.201801418>.
2. Deng, Y., Zheng, X., Bai, Y., Wang, Q., Zhao, J., and Huang, J. (2018). Surfactant-controlled ink drying enables high-speed deposition of perovskite films for efficient photovoltaic modules. *Nat. Energy* *3*, 560-566. 10.1038/s41560-018-0153-9.
3. Bai, S., Da, P., Li, C., Wang, Z., Yuan, Z., Fu, F., Kawecki, M., Liu, X., Sakai, N., Wang, J.T., et al. (2019). Planar perovskite solar cells with long-term stability using ionic liquid additives. *Nature* *571*, 245-250. 10.1038/s41586-019-1357-2.
4. Du, M., Zhu, X., Wang, L., Wang, H., Feng, J., Jiang, X., Cao, Y., Sun, Y., Duan, L., Jiao, Y., et al. (2020). High-Pressure Nitrogen-Extraction and Effective Passivation to Attain Highest Large-Area Perovskite Solar Module Efficiency. *Adv. Mater.* *32*, 2004979. <https://doi.org/10.1002/adma.202004979>.
5. Dong, Q., Zhu, C., Chen, M., Jiang, C., Guo, J., Feng, Y., Dai, Z., Yadavalli, S.K., Hu, M., Cao, X., et al. (2021). Interpenetrating interfaces for efficient perovskite solar cells with high operational stability and mechanical robustness. *Nat. Commun.* *12*, 973. 10.1038/s41467-021-21292-3.
6. Giannozzi, P., Andreussi, O., Brumme, T., Bunau, O., Buongiorno Nardelli, M., Calandra, M., Car, R., Cavazzoni, C., Ceresoli, D., Cococcioni, M., et al. (2017). Advanced capabilities for materials modelling with Quantum ESPRESSO. *J. Phys.: Condens. Matter* *29*, 465901. 10.1088/1361-648x/aa8f79.
7. Perdew, J.P., Burke, K., and Ernzerhof, M. (1996). Generalized Gradient Approximation Made Simple. *Phys. Rev. Lett.* *77*, 3865-3868. 10.1103/PhysRevLett.77.3865.
8. Dudarev, S.L., Botton, G.A., Savrasov, S.Y., Humphreys, C.J., and Sutton, A.P. (1998). Electron-energy-loss spectra and the structural stability of nickel oxide: An LSDA+U study. *Phys. Rev. B* *57*, 1505-1509. 10.1103/PhysRevB.57.1505.
9. Freysoldt, C., Neugebauer, J., and Van de Walle, C.G. (2009). Fully Ab Initio Finite-Size Corrections for Charged-Defect Supercell Calculations. *Phys. Rev. Lett.* *102*, 016402. 10.1103/PhysRevLett.102.016402.
10. Pei, M., Dong, Q., Wang, M., Wang, Y., Ma, H., Liu, J., Wang, R., Bian, J., and Shi, Y. (2022). Accelerating Photogenerated Hole Tunneling through Passivation Layers via Reducing Interplanar Spacing for Efficient and Stable Perovskite Solar Cells. *ACS Appl. Mater. Interfaces* *14*, 16920-16927. 10.1021/acsami.2c02250.
11. Cui, J., Meng, F., Zhang, H., Cao, K., Yuan, H., Cheng, Y., Huang, F., and Wang, M. (2014). CH₃NH₃PbI₃-Based Planar Solar Cells with Magnetron-Sputtered Nickel Oxide. *ACS Appl. Mater. Interfaces* *6*, 22862-22870. 10.1021/am507108u.
12. Wang, K.C., Shen, P.S., Li, M.H., Chen, S., Lin, M.W., Chen, P., and Guo, T.F. (2014). Low-temperature sputtered nickel oxide compact thin film as effective electron blocking layer for mesoscopic NiO/CH₃NH₃PbI₃ perovskite heterojunction solar cells. *ACS Appl. Mater. Interfaces* *6*, 11851-11858. 10.1021/am503610u.
13. Park, J.H., Seo, J., Park, S., Shin, S.S., Kim, Y.C., Jeon, N.J., Shin, H.-W., Ahn, T.K., Noh, J.H., Yoon, S.C., et al. (2015). Efficient CH₃NH₃PbI₃ Perovskite Solar Cells Employing Nanostructured p-Type NiO Electrode Formed by a Pulsed Laser Deposition. *Adv. Mater.* *27*, 4013-4019.

- <https://doi.org/10.1002/adma.201500523>.
14. Chen, W., Wu, Y., Yue, Y., Liu, J., Zhang, W., Yang, X., Chen, H., Bi, E., Ashraful, I., Grätzel, M., and Han, L. (2015). Efficient and stable large-area perovskite solar cells with inorganic charge extraction layers. *Science* **350**, 944. 10.1126/science.aad1015.
 15. Lai, W.-C., Lin, K.-W., Wang, Y.-T., Chiang, T.-Y., Chen, P., and Guo, T.-F. (2016). Oxidized Ni/Au Transparent Electrode in Efficient CH₃NH₃PbI₃ Perovskite/Fullerene Planar Heterojunction Hybrid Solar Cells. *Adv. Mater.* **28**, 3290-3297. <https://doi.org/10.1002/adma.201504621>.
 16. Park, I.J., Kang, G., Park, M.A., Kim, J.S., Seo, S.W., Kim, D.H., Zhu, K., Park, T., and Kim, J.Y. (2017). Highly Efficient and Uniform 1 cm² Perovskite Solar Cells with an Electrochemically Deposited NiO_x Hole-Extraction Layer. *ChemSusChem* **10**, 2660-2667. <https://doi.org/10.1002/cssc.201700612>.
 17. Li, G., Jiang, Y., Deng, S., Tam, A., Xu, P., Wong, M., and Kwok, H.S. (2017). Overcoming the Limitations of Sputtered Nickel Oxide for High-Efficiency and Large-Area Perovskite Solar Cells. *Adv. Sci.* **4**, 1700463. 10.1002/advs.201700463.
 18. Wu, Y., Xie, F., Chen, H., Yang, X., Su, H., Cai, M., Zhou, Z., Noda, T., and Han, L. (2017). Thermally Stable MAPbI₃ Perovskite Solar Cells with Efficiency of 19.19% and Area over 1 cm² achieved by Additive Engineering. *Adv. Mater.* **29**, 1701073. 10.1002/adma.201701073.
 19. Sun, J., Lu, J., Li, B., Jiang, L., Chesman, A.S.R., Scully, A.D., Gengenbach, T.R., Cheng, Y.-B., and Jasieniak, J.J. (2018). Inverted perovskite solar cells with high fill-factors featuring chemical bath deposited mesoporous NiO hole transporting layers. *Nano Energy* **49**, 163-171. 10.1016/j.nanoen.2018.04.026.
 20. Seo, S., Jeong, S., Bae, C., Park, N.G., and Shin, H. (2018). Perovskite Solar Cells with Inorganic Electron- and Hole-Transport Layers Exhibiting Long-Term (approximately 500 h) Stability at 85 degrees C under Continuous 1 Sun Illumination in Ambient Air. *Adv. Mater.* **30**, 1801010. 10.1002/adma.201801010.
 21. Aydin, E., Troughton, J., De Bastiani, M., Ugur, E., Sajjad, M., Alzahrani, A., Neophytou, M., Schwingenschlögl, U., Laquai, F., Baran, D., and De Wolf, S. (2018). Room-Temperature-Sputtered Nanocrystalline Nickel Oxide as Hole Transport Layer for p-i-n Perovskite Solar Cells. *ACS Appl. Energy Mater.* **1**, 6227-6233. 10.1021/acs.aem.8b01263.
 22. Mali, S.S., Kim, H., Kim, H.H., Shim, S.E., and Hong, C.K. (2018). Nanoporous p-type NiO_x electrode for p-i-n inverted perovskite solar cell toward air stability. *Mater. Today* **21**, 483-500. <https://doi.org/10.1016/j.mattod.2017.12.002>.
 23. Abzieher, T., Moghadamzadeh, S., Schackmar, F., Eggers, H., Sutterlüt, F., Farooq, A., Kojda, D., Habicht, K., Schmager, R., Mertens, A., et al. (2019). Electron-Beam-Evaporated Nickel Oxide Hole Transport Layers for Perovskite-Based Photovoltaics. *Adv. Energy Mater.* **9**, 1802995. 10.1002/aenm.201802995.
 24. Boyd, C.C., Shallcross, R.C., Moot, T., Kerner, R., Bertoluzzi, L., Onno, A., Kavadiya, S., Chosy, C., Wolf, E.J., Werner, J., et al. (2020). Overcoming Redox Reactions at Perovskite-Nickel Oxide Interfaces to Boost Voltages in Perovskite Solar Cells. *Joule* **4**, 1759-1775. <https://doi.org/10.1016/j.joule.2020.06.004>.
 25. Eggers, H., Schackmar, F., Abzieher, T., Sun, Q., Lemmer, U., Vaynzof, Y., Richards, B.S., Hernandez-Sosa, G., and Paetzold, U.W. (2020). Inkjet-Printed Micrometer-Thick Perovskite Solar Cells with Large Columnar Grains. *Adv. Energy Mater.* **10**, 1903184. <https://doi.org/10.1002/aenm.201903184>.

26. Zhumagali, S., Isikgor, F.H., Maity, P., Yin, J., Ugur, E., De Bastiani, M., Subbiah, A.S., Mirabelli, A.J., Azmi, R., Harrison, G.T., et al. (2021). Linked Nickel Oxide/Perovskite Interface Passivation for High-Performance Textured Monolithic Tandem Solar Cells. *Adv. Energy Mater.* *11*, 2101662. <https://doi.org/10.1002/aenm.202101662>.
27. Zhang, S., Wang, H., Duan, X., Rao, L., Gong, C., Fan, B., Xing, Z., Meng, X., Xie, B., and Hu, X. (2021). Printable and Homogeneous NiO_x Hole Transport Layers Prepared by a Polymer-Network Gel Method for Large-Area and Flexible Perovskite Solar Cells. *Adv. Funct. Mater.* *31*, 2106495. <https://doi.org/10.1002/adfm.202106495>.